

Alma Mater Studiorum Università di Bologna
Archivio istituzionale della ricerca

Deformation and temperature variation along thrust-sense shear zones in the hinterland-foreland transition zone of collisional settings: A case study from the Barbagia Thrust (Sardinia, Italy)

This is the final peer-reviewed author's accepted manuscript (postprint) of the following publication:

Published Version:

Petroccia, A., Carosi, R., Montomoli, C., Iaccarino, S., Vitale Brovarone, A. (2022). Deformation and temperature variation along thrust-sense shear zones in the hinterland-foreland transition zone of collisional settings: A case study from the Barbagia Thrust (Sardinia, Italy). JOURNAL OF STRUCTURAL GEOLOGY, 161, 1-18 [10.1016/j.jsg.2022.104640].

Availability:

This version is available at: <https://hdl.handle.net/11585/903841> since: 2022-11-18

Published:

DOI: <http://doi.org/10.1016/j.jsg.2022.104640>

Terms of use:

Some rights reserved. The terms and conditions for the reuse of this version of the manuscript are specified in the publishing policy. For all terms of use and more information see the publisher's website.

This item was downloaded from IRIS Università di Bologna (<https://cris.unibo.it/>).
When citing, please refer to the published version.

(Article begins on next page)

This is the final peer-reviewed accepted manuscript of:

Petroccia, A; Carosi, R; Montomoli, C; Iaccarino, S; Vitale Brovarone, A:
*Deformation and temperature variation along thrust-sense shear zones in the
hinterland-foreland transition zone of collisional settings: A case study from the
Barbagia Thrust (Sardinia, Italy)*

JOURNAL OF STRUCTURAL GEOLOGY VOL. 161 ISSN 0191-8141

DOI: 10.1016/j.jsg.2022.104640

The final published version is available online at:

<https://dx.doi.org/10.1016/j.jsg.2022.104640>

Terms of use:

Some rights reserved. The terms and conditions for the reuse of this version of the manuscript are specified in the publishing policy. For all terms of use and more information see the publisher's website.

This item was downloaded from IRIS Università di Bologna (<https://cris.unibo.it/>)

When citing, please refer to the published version.

**Deformation and temperature variation along thrust-sense shear zones in the
hinterland-foreland transition zone of collisional settings: a case study from the
Barbagia Thrust (Sardinia, Italy)**

Petroccia A.^{a*}, Carosi R.^a, Montomoli C.^{a,d}, Iaccarino S.^a & Vitale Brovarone A.^{b,c,d}

^a Dipartimento di Scienze della Terra, Università di Torino, Via Valperga Caluso 35, 10125, Torino, Italy

^b Dipartimento di Scienze Biologiche, Geologiche e Ambientali, Alma Mater Studiorum Università di Bologna, Piazza di Porta San Donato
1, 40126, Bologna, Italy

^c Sorbonne Université, Muséum National d'Histoire Naturelle, UMR CNRS 7590, IRD, Institut de Minéralogie, de Physique des Matériaux
et de Cosmochimie, IMPMC, 4 Place Jussieu, 75005, Paris, France

^d Institute of Geosciences and Earth Resources, National Research Council of Italy, Pisa, Italy

*Corresponding author: alessandrogiovannimichele.petroccia@unito.it

Abstract

In the Internal Zone of a continental collisional orogen, first-order contractional shear zones accommodate crustal shortening. Structural investigations at different scales, flow kinematics, and finite strain analyses are fundamental tools to determine how deformation is accommodated and partitioned. Spatial temperature variations can be responsible for the dynamic weakening and strain localization in the crust, therefore understanding the thermal conditions of shearing and deformation is critical. We integrate field observations, meso- and microstructural analyses, kinematic vorticity estimations, and finite strain data with a quantitative thermometric analysis by Raman spectroscopy on carbonaceous material along a ductile shear zone: the Barbagia Thrust (BT) in the hinterland-foreland transition zone of the Sardinian Variscan belt. These analyses, performed in two different parts of the shear zone, yield similar finite strain gradients, albeit with an increasing component of simple shear with increasing temperature, highlighting the feedback between temperature and vorticity. Our results are best by a tectonic scenario with shear heating, where higher magnitude gradients correspond to higher vorticity and finite strain values, which indicate greater shear and heating values. The heating quantified along the BT is compared favorably to numerical and mechanical models (~ 50 °C). We demonstrate how the BT represents a major tectonic boundary separating the internal sector belonging to the metamorphic core of the belt from the external one involved in the orogenic wedge system.

Keywords:

Shear zone; kinematic vorticity; RSCM; Variscan belt; Nappe Zone

1. Introduction

The geodynamic evolution of collisional orogens has been classically described using an orogenic wedge model, where different rock packages experience different finite metamorphic histories (e.g., Platt, 1993; Jaquet et al., 2018; Malavieille et al., 2019). The hinterland-foreland transition zone making the fold-and-thrust belt is defined by the progressive transition from tectonic units occurring in the metamorphic core of the belt to the ones deformed at shallower crustal levels and steadily included in the orogenic wedge (Larson et al., 2010; Thigpen et al., 2010,

2017; Schneider et al., 2014; Montomoli et al., 2018). The first theoretical models applied to the hinterland-foreland transition zone were initially developed within a critical-wedge framework wherein thrust behavior is dominantly brittle and occurs along discrete planes (e.g., Elliott, 1976; Dahlen et al., 1984). Recent, it is well-noted that during orogenic belt formation, large sectors of crustal rocks exhibit ductile and brittle-ductile deformation (e.g., Platt, 1986; Grasemann et al., 1999; Steck, 2008; Steck et al., 2013; Jaquet et al., 2018).

Hinterland-foreland transition zones are characterized by the presence of mylonitic rocks along km-scale ductile shear zones linked to thrust-sense shear zones, which lead to the formation of thrust sheets or tectonic nappes. Classically, these zones have been associated with a simple shear-dominated deformation (e.g., Coward and Kim, 1981; Mitra, 1994; Seno et al., 1998; Yonkee, 2005). However, quantitative studies have shown that the ductile deformation in the thrust-sense shear zone involves a significant component of pure shear deformation (e.g., Simpson and De Paor, 1993; Grasemann et al., 1999; Ring and Brandon, 1999; Bailey et al., 2007; Ring and Kumerics, 2008; Law et al., 2021). Therefore, shear zones in dynamics orogenic wedge settings require a quantitative assessment of the kinematic vorticity (Xypolias, 2010; Thigpen et al., 2010, 2013; Fossen and Cavalcante, 2017; Ghosh et al., 2020; Simonetti et al., 2020a, b).

Several processes can potentially be responsible for the dynamic weakening and strain localization in the crust, including (i) shear heating (e.g., Brun and Cobbold, 1980; Molnar and England, 1990; Camacho et al., 2001; Burg and Schmalholz, 2008; Thielmann and Kaus, 2012; Platt, 2015, 2018; Regenauer-Lieb et al., 2015), (ii) fabric development (e.g., Montési, 2013), and (iii) grain-size reduction by cataclasis or dynamic recrystallization (e.g., Montési and Zuber, 2002; Handy et al., 2007; Platt and Behr, 2011). Among them, thermal weakening (Takeuchi and Fialko, 2012; Willis et al., 2019), linked to shear heating, has been regarded as one of the main mechanisms in localizing deformation and for the development of shear zones (e.g., Schott et al., 2000; Thielmann and Kaus, 2012; Duretz et al., 2014). This mechanism is particularly applicable to the middle crust close to the brittle/ductile transition (e.g., Hirth et al., 2001; Behr and Platt, 2014; Platt, 2015). Thus, establishing the thermo-kinematic setting of shear zones is crucial because it is one of the most effective ways to test theoretical models of orogen-

tectonometamorphic evolution against field observations (e.g., Sanderson, 1982; Ring et al., 2001; Law et al., 2004; Thigpen et al., 2021; Iaccarino et al., 2020; Waters et al., 2018).

Several works have used a multidisciplinary approach to unravel the deformational, structural, and thermal gradients of a region and, in turn, discriminate marginal and central areas within high strain shear zones (Xypolias, 2010; Ring et al., 2015; Carosi et al., 2020; Grujic et al., 2020; Simonetti et al., 2020a, b, 2021). Field-based studies, combined with vorticity and kinematic analysis, are key for exploring shear zone evolution. There are several analytical techniques to determine both the kinematic vorticity and the deformation temperature in mylonitic rocks. Whereas kinematic vorticity estimation can be generally obtained from all kinds of deformed rocks, low-grade metasedimentary sequences in the hinterland-foreland transition zone contain mineralogical assemblages that are not always suitable for conventional thermometric techniques.

The Raman spectroscopy on carbonaceous material (RSCM; Beyssac et al., 2002, 2003, 2004) is based on the progressive transformation of carbonaceous material (CM) to graphite with increasing temperature. RSCM has generally been used as a geothermometer to determine the peak temperature reached during burial or tectonic thrust stacking (Chen et al., 2011; Scharf et al., 2013; Vitale Brovarone et al., 2013; Bellanger et al., 2015; Molli et al., 2018; Berger et al., 2020; Pérez-Cáceres et al., 2020; Montmartin et al., 2021; Nibourel et al., 2021), during contact metamorphism (Aoya et al., 2010; Mori et al., 2017; Beyssac et al., 2019; Skrzypek, 2021) or during frictional heating along fault planes after an earthquake (Fauconnier et al., 2014; Kaneki et al., 2016; Kuo et al., 2017, 2018; Nakamura et al., 2020; Muirhead et al., 2021). It is non-destructive and sensitive to thermal changes, enabling to constrain peak temperature in rocks from different geological contexts and metamorphic conditions (see Henry et al., 2019 for a complete review).

The hinterland-foreland transition zone of the Sardinian Variscan belt in Italy is a well-preserved low- to medium-grade Variscan basement that was not overprinted by subsequent Alpine orogenesis. It represents an excellent site to investigate a regional thrust-sense movement shear zone related to the nappe emplacement during the continental collision in the Early Carboniferous, i.e., the Barbagia Thrust (BT; Carosi and Pertusati, 1990; Carosi and Malfatti, 1995; Montomoli et al., 2018). The BT marks the boundary between the Internal and the External

Nappe Zone of the Variscan belt, separating tectonic units with a complex pressure-temperature-time (P-T-t) history from tectonic units deformed at a higher structural level during the progressive propagation of deformation from the hinterland to the foreland (Montomoli et al., 2018). It played a critical role during nappe stacking and the exhumation of the crustal units. Few studies have addressed the structure, kinematics, and flow regime of the BT (e.g., Montomoli et al., 2018), and its thermal architecture is poorly understood.

To better constrain the structural architecture and the thermal evolution of the BT, we collected data in two thermally- and potentially kinematically-distinct sectors of the shear zone. In this study, we defined the thermo-structural evolution of the BT within the Nappe Zone by combining detailed field observations, meso- and microstructural analysis, vorticity analysis, and finite strain estimations with a quantitative thermometric analysis by RSCM. Variations in both temperature conditions of shearing and magnitude of simple shear between these two domains allow us to examine any linkages and feedbacks between shear heating and thrust kinematics.

2. Overview of the Sardinian Variscan belt

The continent-continent collision between Laurentia–Baltica and Gondwana is responsible for the deformation of the Sardinian Paleozoic basement (Carmignani et al., 1994) during the Variscan orogeny (Matte, 2001). The Sardinian metamorphic belt (Carmignani et al., 2001, 2015; see Cruciani et al., 2015 for a review) is made up of: (i) the External Zone, (ii) the Axial Zone or the hinterland of the belt and (iii) the Nappe Zone or hinterland-foreland transition zone (Fig. 1a).

(insert Figure 1 here)

The Nappe Zone of central and southern Sardinia has received considerable attention over the last 40 years (Carmignani and Pertusati, 1977; Carmignani et al., 1982, 1994, 2015; Carosi et al., 1991; Conti et al., 1998, 1999, 2001; Franceschelli et al., 2005; Casini et al., 2010; Cocco and Funedda, 2011, 2017; Cocco et al., 2018). It has been subdivided into External (central to southern Sardinia) and Internal (northern to central Sardinia) Nappe Zone (Fig. 1a). The lithostratigraphic succession is similar in both nappes. The main difference is the relative paucity of

Ordovician metavolcanic rocks in the Internal Nappe Zone sequence (Carmignani et al., 1994) compared to the External Nappe Zone.

The Internal Nappe Zone (Fig. 1a) comprises: (i) the Low-Grade Metamorphic Complex (LGMC; Barbagia, Goceano, and southern Nurra units; Vai and Cocozza, 1974; Carmignani et al., 1994; Pertusati et al., 2002; Montomoli, 2003) which reached greenschist-facies metamorphic conditions, and (ii) the Medium-Grade Metamorphic Complex (MGMC; Baronie, Anglona, and northern Nurra units; Carmignani et al., 1994, 2001) which reached amphibolite-facies conditions (Cruciani et al., 2015; Carosi et al., 2020). The boundary zone between the Internal Nappe Zone and the High-Grade Metamorphic Complex is marked by the Posada-Asinara shear zone (PASZ; Carosi et al., 2020 and references therein; Fig. 1a), a dextral transpressive Late-Variscan shear zone (Carosi et al., 2002), active from ~325 up to ~300 Ma (Di Vincenzo et al., 2004; Carosi et al., 2012; 2020).

In the External Nappe Zone, five main tectonic units have been identified, which include according to the lowest to the highest unit in the pile (Fig. 1b): (1) Monte Grighini Unit, (2) Riu Gruppa/Castello Medusa Unit, (3) Gerrei Unit, (4) Meana Sardo Unit and, finally, (5) Sarrabus Unit (Calvino, 1959; Carosi et al., 1991; Musumeci, 1992; Carmignani et al., 1994; Conti et al., 2001; Barca et al., 2003; Funedda et al., 2011, 2015; Pavanetto et al., 2012; Cocco et al., 2018). All these units are characterized by syn-tectonic regional greenschist-facies metamorphism (Carmignani et al., 1994; Carosi et al., 1991, 2010; Franceschelli et al., 1992), except for the Monte Grighini Unit. Illite and chlorite crystallinity values report anchizonal-epizonal metamorphic conditions for the External Nappe Zone (Franceschelli et al., 1992; Carosi et al., 2010; Montomoli et al., 2018). The boundary between the Internal and the External nappes is defined by a regional-scale thrust-sense shear zone that developed a pervasive high-strain mylonitic zone, i.e., the BT (Carosi and Malfatti, 1995; Montomoli et al., 2018).

Several authors have documented a complex structural evolution of both Internal and External Nappe Zone (Carmignani and Pertusati, 1977; Carmignani et al., 1982, 1994; Dessau et al., 1982; Carosi and Pertusati, 1990; Carosi et al., 1991, 2002, 2004; Conti and Patta, 1998; Conti et al., 1998; Funedda, 2009; Montomoli et al., 2018). D₁ and D₂ deformation phases are related to continental collision and thrust related shortening, responsible for nappe emplacement. These are followed by later D₃ and D₄ tectonic phases (Conti et al., 1998, 2001; Carosi et al.,

2002, 2004) that represent the end of the collisional shortening (D_3 phase) and the collapse of the belt (D_4 phase). The latter is regarded as nearly contemporaneous with the emplacement of the Sardo-Corso batholith at ~320-280 Ma (Del Moro et al., 1975; Casini et al., 2012).

We focused on two key sectors, Area I and II, for the northern and the southern investigated selected areas, respectively (Fig. 1b), of the hinterland-foreland transition zone (Fig. 1b). Here, the contact between the Internal and External Nappe Zone (i.e., the Barbagia Thrust) is marked by a well-exposed mylonitic zone. Both areas are located in the Barbagia region (Central Sardinia), along with the northern and the southern limb of the Barbagia Synform (Fig. 1b, c). Area I and II are ~20 km apart. The Internal Nappe Zone is represented by the structurally upper Barbagia Unit (BU), in the hangingwall (HW), overthrust on the Meana Sardo Unit (MSU), in the footwall (FW), belonging to the External Nappe Zone (Fig. 1b, c). The structural maps, the cross-sections, the projection of structural data, and the position of the analyzed samples are reported in Figure 2a,b and in Figure 3a,b.

(insert Figure 2 here)

3. Meso- and microstructural analysis results

In both Area I and II, four main phases of ductile deformation were observed based on overprinting criteria and structural observations from the meso- to microscale. Microstructural analyses were performed on field-oriented samples, cut perpendicular to the main foliation and parallel to the object lineation (approximating the XZ section of the finite strain ellipsoid). Folds have been described following Ramsay (1967). Dynamic deformation mechanisms for both quartz and feldspar have been described according to Pryor (1993), Piazzolo and Passchier (2002), Stipp et al. (2002) and Law (2014). Foliations, kinematic indicators, and mylonites have been classified according to Passchier and Trouw (2005). Mylonite has been classified considering the percentage of the matrix as compared to porphyroclasts, varying from 50-90% for mylonitic rocks to more than 90% for ultramylonite. Mineral abbreviations are after Whitney and Evans (2010) except for white mica (Wm).

(insert Figure 3 here)

3.1. D_1 and D_2 deformation phases

Relicts of the original bedding (S_0) can be recognized as a compositional alternation (Fig. 4a) or dismembered lentoid fragments only far from the BT. D_1 phase is well-expressed far from the BT and mainly in FW. Fold systems related to the D_1 phase are only observed in Area II within the External Nappe Zone, far from the BT. They show a S-SW vergence (Fig. 4b) and are moderately to strongly asymmetric. In most cases, the D_1 signature is represented by the S_1 foliation, parallel or at a moderate angle to the bedding (S_0 ; Fig. 4b). Often, due to complete transposition, it is nearly impossible to distinguish S_1 from S_0 ($S_1//S_0$). The S_1 can be recognized within the thickened hinges of F_2 folds and in microlithons (Fig. 4c). At the microscale, S_1 is a continuous foliation defined by syn-kinematic recrystallization of white mica (Fig. 4c), chlorite, quartz, calcite, opaque minerals, and rare albite. Moving toward the BT high-strain zone, a well-developed transposition of S_1 and rootless folds (Fig. 4d) has been recognized.

Structures related to the D_2 phase are characterized by tight to isoclinal, overturned to recumbent folds, with a S-SW vergence, developed from micro- to map-scale. The interlimb angles of F_2 folds range from $60-2^\circ$ (close to sub-isoclinal; Fig. 4d), and they generally show rounded and thickened hinges with stretched limbs (class 2 of Ramsay, 1967; Fig. 4d). The F_2 folds show an S_2 foliation parallel or sub-parallel to the relative fold axial planes, and it generally represents the main foliation at the outcrop-scale. S_2 mainly strikes E-W with both local NNW-SSE and NNE-SSW. In Area I, S_2 dips to the S with local variations toward the N (Fig. 2a) due to late deformation, while in Area II (Fig. 3a), S_2 dips toward the N. F_2 fold axes show the main E-W trend gently plunging with quite scattered values in both Area I and II (Fig. 2b, 3b). A well-visible N-S or NE-SW trend (Fig. 2b, 3b) of the object lineation L_2 on the S_2 foliation is recognizable (Fig. 4e). The F_2 fold axes are nearly perpendicular to the L_2 . Moving toward the BT, the main anisotropy gradually changes from a gradational to discretely spaced crenulation cleavage to a continuous S_2 foliation defined mainly by chlorite + white mica (Fig. 4f). The intensity of strain increases toward the tectonic contact, as does the mylonitic foliation. It is worth noting that the frequency of the occurrence of the D_1 structures decreases approaching the BT.

(insert Figure 4 here)

3.2. The Barbagia Thrust

In both Area I and II, located along the northern and southern limb of the Barbagia Synform, the BT is characterized by a hm-thick mylonitic zone that shows a similar deformation pattern. The BT-related structures (D_2) overprint both metasedimentary and metavolcanic or metavolcanoclastic rocks of the FW and metasandstone, metasilstone, and metapsammite of the HW (see the geological maps in Figs. 2a and 3a), transposing all previous structures. In the FW and HW of the BT, a variation in structural style moving toward the BT across the deformation gradient is present. The intensity of deformation increases toward the BT, where folds become tighter and lineation more pervasive; contemporaneously, the spacing between foliation domains decreases. Approaching the high strain zone, the mylonitic foliation obliterates the previous S_1 foliation and microlithons. Although Area I and II are located in different sectors of the F_3 Barbagia Synform, they are characterized by the same shear sense. Sheared metasedimentary rocks belonging to the FW (San Vito Fm.) and the HW (Filladi del Gennargentu Fm.) are characterized by a transition from a well-developed discrete smooth spaced foliation with zonal cleavage domains (Fig. 5a) up to a continuous cleavage (Fig. 5b) approaching the BT. In samples from the high-strain zone, a penetrative continuous mylonitic foliation is found. The mylonitic S_2 foliation is defined by elongated quartz grains and phyllosilicate-rich levels, dominated by chlorite + white mica (Fig. 5b). Patchy undulose extinction (Fig. 5c) and small new grains are recognizable in quartz. These structures suggest that bulging mechanisms (BLG II) with minor and local subgrain rotation recrystallization (SGR; Fig. 5d) are the main deformation mechanisms in quartz (Stipp et al., 2002; Law, 2014). Kinematic indicators with a top-to-the S/SW sense are represented by a meso- (Fig. 5e) and microscale (Fig. 5f) C' - S fabric, asymmetric porphyroclasts and rare asymmetric displacement-controlled strain fringes around rigid objects, mainly constituted by pyrite. In the FW, metavolcanic and metavolcanoclastic rocks belonging to the Santa Vittoria Fm., a progressive transition from non-sheared rocks to mylonites (Fig. 5g) to ultramylonites (Fig. 5h) can be observed along the deformation gradient approaching the BT. This is coupled with a gradual variation from a disjunctive cleavage with sub-parallel cleavage domains to a continuous cleavage in the most intensely deformed ultramylonitic rocks. In mylonites, the main foliation is defined by grain shape preferred orientation of feldspar, quartz, white mica, and chlorite (Fig. 5g). Feldspars show undulose extinction, evidence of brittle deformation, and locally flame perthite. In

ultramylonite, the matrix is composed of ultra-fine-grained black bands made by phase-mixing of white mica surrounding rounded K-feldspar (Fig. 5h) and plagioclase porphyroclasts. The fine grain size ($< 25 \mu\text{m}$) of quartz in these rocks prohibits the identification of their recrystallization mechanisms. Kinematic indicators include C' -S fabrics, mica fish, and the asymmetry of porphyroclasts (Fig. 5h) of quartz or feldspar crystals which indicate a top-to-the S-SW sense of shear.

(insert Figure 5 here)

3.3. D_3 and D_4 deformation phases

The D_3 phase is composed of m- to km-scale folds (i.e., Gennargentu Antiform and Barbagia Synform) that overprint and refold all previous structural elements, including the BT (Fig. 6a). They are commonly gentle, slightly asymmetric, and open, ranging from upright to steeply inclined and from metric to pluri-m long wavelengths (Fig. 6a, b). Locally kink type folds occur (Fig. 6c). These folds display a S-SE vergence (Fig. 6a, b, c) with local variation to N. A_3 axes generally are coaxial to the A_2 axes and perpendicular to the L_2 object lineation in both investigated areas (Figs. 2b and 3b). In the F_3 hinge zones of less competent units, the S_3 axial-plane foliation is represented by a gradational crenulation cleavage (Fig. 6d). The main deformation mechanisms, as seen at the microscale, are pressure solution and kinking in phyllosilicate-rich domains (Fig. 6e). No metamorphic mineral assemblage related to these folds has been observed (Fig. 6e). D_4 produced gentle to open F_4 folds with sub-horizontal axes and axial planes (Fig. 6f). Locally, some minor-scale kink-folds occur. No metamorphic mineral assemblages related to the D_4 phase have been observed.

(insert Figure 6 here)

4. Kinematic vorticity and finite strain results

In order to characterize the type of flow within the BT, kinematic vorticity analyses were performed on mylonitic samples in both Area I and II (Figs. 2a and 3a). In the present study, the C' shear band method (Kurz and Northrup, 2008; Gillam et al., 2013) and two different porphyroclast-based methods, the porphyroclast aspect ratio method (PAR; Passchier, 1987; Wallis et al., 1993) and the rigid grain net method (RGN; Jessup et al., 2007), have been

applied. See Appendix 1 for a detailed description of the different methods. A total of 19 samples (8 for HW and 11 for FW) were selected (Table 1). Examples of polar histograms related to C' shear band method (sample AP19-37), used to derive the angle ν , are provided in Figure 7a. For the RGN and PAR methods, an example of the same sample (sample AP19-37) is shown in Figure 7b, c, respectively. An example (sample AP19-39B) of the Fry diagram for both the XZ and YZ sections of the finite strain ellipsoid is presented in Figure 7d. Full results are provided in Appendix 2, 3, and 4. The complete finite strain dataset (samples locations in Figs. 2a and 3a), obtained by the centre-to-centre method, is reported in Table 1.

(insert Figure 7 and Table 1 here)

4.1. Area I

In Area I, a total of 9 samples (3 for HW and 6 for FW, respectively; Fig. 2a) analyzed with the C' shear band method gives (Table 1) a vorticity number ranging from 0.50 to 0.93, with a mean of 0.71. In sample AP19-37, from the FW, we found, applying the stable porphyroclasts method, a minimum R_c of 1.98 and a maximum R_c of 2.20 corresponding to W_k values of 0.59 and 0.66 (Table 1), respectively. In sample LA-14, from the FW, minimum and maximum R_c values are 2.11 and 2.33, corresponding to W_k between 0.63 and 0.69 (Table 1). The overlapping but different range of vorticity (Fig. 8a) in these samples may be due to (i) different analytical uncertainties associated with input data and/or (ii) the different strain memory. Finite strain results in Area I indicate an axial ratio of 2.18, 2.65, and 3.30 on the XZ sections, 1.42, 1.62, and 1.26 on YZ sections of the finite strain ellipsoid and the shape parameter of the strain ellipsoid (K) is 1.27, 1.03 and 6.23 for samples AP19-125, AP19-39B, and 2021_81A, respectively (Fig. 7b). Mylonite in the middle part of the shear zone (samples AP19-39B) is close to plane strain conditions, whereas mylonite closest to the core of the BT (sample 2021_81A) is in the prolate field (Fig. 7c).

4.2. Area II

Data from Area II, obtained from 9 samples analyzed by the C' shear band method (5 for HW and 4 for FW, respectively; see Fig. 3a for sample location and Table 1 for results), give a vorticity number ranging from 0.50 to

0.90, with a mean of 0.67. In Area II, finite strain results indicate an axial ratio of 1.96, 2.25, and 2.42 on the XZ sections and 1.49, 1.63, 1.36 on YZ sections of the finite strain ellipsoid and the shape parameter of the strain ellipsoid (K) is 0.39, 0.61 and 2.17 for samples 2021_56B, 2021_56A, and 2021_40B, respectively. In the Flinn diagram (Fig. 8b), the two farthest samples with respect to the core of the BT (samples 2021_56A and 2021_56B) fall in the oblate field near the plane strain conditions. Finite strain in mylonite in the external part of the shear zone (AP19-125) plots close to plane strain conditions, whereas in samples closest to the core of the BT (sample 2021_40B) is in the prolate field (Fig. 7c).

Estimated values in both Area I and II reveal an important contribution of pure shear during thrust-sense ductile deformation (Fig. 8a). Moreover, the results highlight in both areas, a strong increase of the component of simple shear along the deformation gradient in both units, approaching the BT high-strain zone (Fig. 8a, Table 1).

(insert Figure 8 here)

5. RSCM estimates

The peak temperature was obtained using RSCM. This method is based on the progressive transformation of CM during the increase of temperature, and it is not affected by the retrograde history (Beyssac et al., 2002; Beyssac and Lazzeri, 2012). The RSCM temperature estimates, discussed in the following sections, were derived from the Aoya et al. (2010) calibration (see Appendix 1 for a detailed description of the RSCM procedure). The temperature results, calculated with both Beyssac et al. (2002) and Aoya et al. (2010) calibrations, are given in Table 1. A total of 18 samples, from both Area I and Area II (Figs. 2a and 3a for sample location) collected at different structural positions, were selected for RSCM analysis. Representative spectra and corresponding RSCM temperatures are reported in Fig. 9a, b, respectively.

(insert Figure 9 here)

5.1. Area I

In Area I, the R2 parameter ranges from 0.30 to 0.41 with an average of 0.35. The R2 parameter varies from 0.30 to 0.40 and from 0.31 to 0.41 for the HW and FW, respectively (Table 1). We detected a systematic increase in temperature moving from the structurally higher parts of the HW, or from the structurally lower parts of the FW, moving into the BT core, from ~455 up to 508 °C (Fig. 9a). In particular, within the HW, temperature increases along the deformation gradient from a minimum of ~454 up to 502 °C close to the BT. The Raman spectra of the FW follow the same pattern and temperature increases from ~444 °C up to ~496 °C for the sample nearest to the BT. The lowest temperatures in Area I have been found in non-mylonitic samples, where relict S_1 foliation is observable in microlithons (Fig. 10a). No systematic differences in the obtained RSCM T results have been detected from graphite lying on S_1 or S_2 . Samples with the highest temperature have been found in mylonitic rocks within the core of the BT (Fig. 10b).

5.2. Area II

In Area II, the R2 parameter ranges from 0.29 to 0.48, with an average of 0.36. The R2 parameter varies from 0.42 to 0.29 and from 0.48 to 0.31 for the HW and FW, respectively (Table 1). Moving from the structurally higher sectors of the HW, or from the structurally lower one of the FW, toward the BT, we highlighted a general increase in temperature, from ~420 up to 505 °C (Fig. 9b). Along the deformation gradient, temperature increases from ~420 up to 497 °C and ~443 up to 505 °C for FW and HW, respectively. As for Area I, the lowest temperatures in Area II have been detected in non-mylonitic samples (Fig. 10a) and no differences have been detected from graphite lying on S_1 or S_2 . Samples with the highest temperature have been found in mylonites from both HW and FW (Fig. 10b).

(insert Figure 10 here)

6. Discussion

6.1. Geometry and deformation regime of the BT

Detailed meso- and microstructural analyses have unravelled the tectonic history of two different sectors (Area I and Area II) of the BT in the Sardinian Variscan belt (Fig. 1b). This region has undergone a polyphase evolution

consisting of four ductile deformation phases. Sedimentary bedding S_0 is only observed in a few areas where a strong lithological contrast is present. The D_1 structures are detectable far from the BT and mainly in the FW. The S_1 foliation is defined by quartz + white mica + chlorite, indicating a greenschists-facies condition. The main structures of the study area are controlled by the D_2 deformation phase. This phase is linked to the syn-nappe stacking and exhumation of the HW (Carosi et al., 2004; Montomoli et al., 2018). We highlight an increase in shear deformation along with the progressive transposition of previous D_1 structures approaching the BT. The observed deformation gradient in Area I appears strikingly similar to that reported along the BT in the Area II (Carosi et al., 2004; Montomoli et al., 2018). The S_2 foliation, parallel to the boundaries of the shear zone, and the F_2 fold axes, perpendicular to the L_2 object lineation, are coeval with the overthrust of the Internal Nappe Zone onto the External Nappe Zone (Carosi et al., 2004). The syn-kinematic mineral assemblage (chlorite + white mica) along the S_2 mylonitic foliation is indicative of greenschist-facies metamorphic conditions. This is in agreement with the main dynamic recrystallization mechanism of quartz, indicative of temperature ranges ~ 400 – 450 °C (BLG II and local SGR; Piazzolo and Passchier 2002; Stipp et al., 2002). These data are corroborated by the presence of undulose extinction, local flame perthite, and brittle deformation in feldspar, indicating ~ 400 – 500 °C (Pryer, 1993). The observed relationships between mineral assemblage growth and deformation and dynamic recrystallization mechanisms are broadly consistent with those reported by Montomoli et al. (2018), but with some differences. Whilst, the syn-kinematic minerals observed during the D_2 phase are the same as previous authors, the observed quartz recrystallization mechanism indicates slightly higher temperatures of deformation. However, the lack of Grain Boundary Migration (GBM) in quartz, as highlighted by Conti et al. (1998), Montomoli et al. (2018), and this work, indicates that deformation probably did not exceed ~ 500 °C. Kinematic indicators, both at the meso- and microscale, in Area I and II, reveal a top-to-the S-SW sense of shear. This also agrees with the S-SW F_2 fold vergence detailed by previous authors (Carosi, 2004; Carosi et al., 2004; Montomoli et al., 2018). The whole architecture of the Nappe Zone is affected by regional-scale F_3 folds (D_3). The D_3 phase is characterized by pressure solution, indicating an upper structural level deformation. Also, the presence of the BT mylonitic zone in the different sectors of the Barbagia Synform, with the same structural and kinematic features, indicates that F_3 folding deformed this tectonic contact. Similar structural results and the same shear sense were obtained from both

zones, confirming the post-nappe stacking folded structure (i.e., Barbagia Synform). Subsequent post-collision extensional tectonics was characterized by the development of open folds (F_4).

6.2. RSCM temperature variation along the BT

Orogenic systems are partially characterized by successive and moderate overprinting thermal events (e.g., Brown, 1993; Delchini et al., 2016; Beyssac et al., 2019). One of them is the progressive increase of temperature along shear zones (Thigpen et al., 2010). There are several methods for investigating the thermal architecture of a low-temperature portion of orogenic belt, including vitrinite reflectance (Ferreiro Mählmann et al., 2012), illite and chlorite crystallinity (Merriman et al., 1995; Jaboyedoff et al., 2001; Maino et al., 2015; Vidal et al., 2016), and RSCM thermometry (Beyssac et al., 2002; Rahl et al., 2005; Aoya et al., 2010; Lahfid et al., 2010; Kouketsu et al., 2014). Montomoli et al. (2018) performed both illite and chlorite crystallinity measurements on samples transecting the BT, but found no systematic changes in those parameters across the structural profile. Compared to the illite and chlorite crystallinity measurements, RSCM thermometer, in the absence of extreme fluid-rock interaction or deformation (Moris-Muttoni et al., 2022 and references therein), may be more sensitive to the temperature variation recording peak temperature (e.g., Beyssac et al., 2002; Lahfid et al., 2010; Aoya et al., 2010). We document RSCM temperatures across the BT on both strongly deformed and weakly deformed samples taken from two different structural sectors of the same shear zone. We highlight an increase in temperature moving from the structurally higher parts of the HW, or from the structurally lower parts of the FW, toward the BT core. The lowest RSCM temperature from non-mylonitic samples of both FW and HW (Fig. 11a, b) is slightly different in Area I and II. Based on the geological framework, this T is linked to the maximum temperature reached during collisional shortening and regional metamorphism in the HW and FW. RSCM temperatures range from ~420 to ~450 °C, in agreement with the documented metamorphic mineral assemblage and recrystallization mechanism of quartz and feldspar. In comparison, mylonites return higher RSCM temperatures ranging from ~470 to ~500 °C (Fig. 10a). The detected RSCM T shift between non-mylonitic to mylonitic rocks is in the range of ~50-70 °C.

Several factors could cause this rise in temperature towards the core of shear zones: (i) graphite precipitation from a hydrothermal fluid; (ii) detrital graphite; (iii) strain reorganization of graphite; and (iv) shear heating. Fluids

have previously been invoked to explain the presence of CM with unusual crystallinity (Skrzypek, 2021; Vitale Brovarone et al., 2020). CM grains found in low-grade metamorphic rocks but indicating higher temperatures have been explained by the precipitation of higher-crystallinity (lower R2) CM from hydrothermal fluids (Křibek et al., 2008) or detrital origin (Galy et al., 2008). Whilst we cannot completely exclude fluid-rock interaction during shear deformation or detrital origin of graphite, the presence of a systematic increase in the CM crystallinity from the boundary to the core of the shear zone, in both areas, and the paucity of meso- and/or microscale evidence for fluids (e.g., veins stockwork) make it to appear unlikely.

The RSCM data reported here show a persistent and systematic increase in T with increasing strain intensity moving into the BT high strain shear zone. Several contributions have demonstrated that strain could reorganize the structure of graphite (Kitamura et al., 2012; Furuichi et al., 2015; Kouketsu et al., 2019; Kedar et al., 2020; Lyu et al., 2020; Nakamura et al., 2015, 2020). This strain-induced mechanism is similar to lattice modification and recrystallization in the ductile deformation of minerals (Wang et al., 2019). If strain could reorganize the structure of the CM, the obtained RSCM T may be not systematic in the temperature increase. However, the strain-driven crystallization of CM is most effective in low-grade metamorphic rocks (~ 200 - 350 °C), where the deformation could strongly modify the internal structure of CM (Wang et al., 2019). Our lowest temperatures have been obtained from non-mylonitic samples and are associated with T of ~ 420 - 450 °C (Fig. 11a), linked to collisional shortening and regional metamorphism. Thus, these samples are characterized by medium crystalline and organized graphite that could be difficult to deform and give us an increase in temperature of ~ 50 - 70 °C due to strain-induced mechanism. Despite this, we cannot completely exclude this factor.

Shear heating has been shown to produce temperature increases in shear zones (Molnar and England, 1990; Camacho et al., 2001; Burg and Gerya, 2005; Mako and Caddick, 2018; Waters et al., 2018; Thigpen et al., 2021). The amount of heat generated during shear heating varies as a result of several factors: (i) convergence rate, (ii) strain rate, and (iii) width. Mako and Caddick (2018) used numerical models to calculate shear heating magnitudes as high as ~ 200 °C, but they suggest that natural shear zones would probably produce much lower values. Thus, several authors (Jamieson and Beaumont, 2013; Mako and Caddick, 2018; Waters et al., 2018; Iaccarino et al.,

2020) highlight that shear heating, in most common natural shear zones, produces relatively little heat compared to the surrounding rocks, probably on the order of $\sim 10\text{--}60\text{ }^{\circ}\text{C}$. In particular, shear heating for low initial temperature ($\sim 300\text{--}400\text{ }^{\circ}\text{C}$) is strongly dependent on convergence velocity (Waters et al., 2018). Shear heating $>100\text{ }^{\circ}\text{C}$ is only achievable with high convergence velocities ($\sim 3\text{--}5\text{ cm/year}$), whereas lower convergence velocities ($\sim 1\text{ cm/year}$) can only produce heating $>50\text{ }^{\circ}\text{C}$, according to the calculations of Mako and Caddick (2018). The strain rate and the width of the shear zone can also play an important role in the potential magnitudes of shear heating (Mako and Caddick, 2018). Integrating the strain rate values obtained by Montomoli et al. (2018) along the BT ($10^{-12}\text{--}10^{-14}\text{ s}^{-1}$) with the measured width of the shear zone in both transects ($\sim 600\text{ m}$) in the Mako and Caddick (2018, their figure 9) graphs, it is possible to predict the potential temperature increase due to shear heating across the BT shear zone. Considering a shear activity ranging between 5-10 Ma and known strain rate values of Montomoli et al. (2018), for non-mylonitic rocks of initial temperature of $\sim 400\text{--}450\text{ }^{\circ}\text{C}$, these integrated models of shear heating predict a T increase of $\sim 50\text{ }^{\circ}\text{C}$. Moreover, the calculations of Mako and Caddick (2018) also imply that the observed maximum-T conditions are only possible for lower convergence velocities ($\leq 3\text{ cm/year}$). In summary, our RSCM T estimates derived both in Area I and II indicate that the temperature shift between the mylonitic and non-mylonitic rocks is approximately $\sim 50\text{--}70\text{ }^{\circ}\text{C}$ (Fig. 11a), in agreement with the numerical simulations. The displacement of the ductile shear zone is directly related to the strain rate, the width of the shear zone (Molnar and England, 1990; Waters et al., 2018), and the thermal architecture. The amount of erosion before the development of the BT is not known. However, temperatures of $\sim 450\text{ }^{\circ}\text{C}$, obtained by the RSCM method in the HW metasediments imply depths of $\sim 18\text{ km}$ when coupled with plausible thermal gradients of $25\text{ }^{\circ}\text{C km}^{-1}$ (Casini et al., 2012; Montomoli et al., 2018). In the above scenario, taking a thrust dip reference value of $\sim 35^{\circ}$, as roughly equivalent to the syn-orogenic dip of the BT, we can calculate the minimum magnitude of displacement of the BT. We obtain $\sim 31\text{ km}$ of displacement (vertical depth/sin(thrust dip angle)), which may represent a first-order estimate for the minimum horizontal displacement on the BT. This result is confirmed by the distance calculated on the basis of cartographic evidence (estimated parallel to the shear plane) of about $\sim 20\text{--}30\text{ km}$, which is comparable to the amount reported by Carosi and Malfatti (1995). As highlighted by different

authors (Burg and Gerya, 2005; Waters et al., 2018), the fault displacement represents another important parameter to be taken into account while discussing shear heating. Along shear zones with a considerable displacement, as in this case, combined with a relatively short duration of ductile shearing, the most plausible heat source is shear heating (Mako and Caddick, 2018). It is also worth noting that, even if the RSCM absolute error is about ± 50 °C (Beyssac et al., 2002, 2004), we detect a systematic thermal increase following the deformation gradient and toward the BT in both Area I and II. Nevertheless, in the southernmost area, the thermal variation from non- to strongly deformed rocks is larger than the absolute error of the method and thus increases the reliability of the obtained data. However, the meaning of the detected thermal gradient across the BT is still uncertain.

Fluid circulation, strain reorganization and shear heating may be equally responsible for the increase in the obtained RSCM temperatures. It is obvious that the driving factor strongly changes the interpretation of the geological data. Nevertheless, due to the magnitude of the recorded increase in temperature that fits well with the model predictions, the obtained results appear to be consistent with a shear heating model. A number of works have documented that shear heating has strongly influenced the thermal structure of shear zones; as the Main Central Thrust in the Himalayas (Molnar and England, 1990), the South Tibetan Detachment System in the Everest region (Waters et al., 2018); for the Central and the Western Alps (Burg and Gerya, 2005; Schmalholz and Duretz, 2015); in the Davenport shear zone, central Australia (Camacho et al., 2001); the Norumbega fault zone, Central Maine (Mako and Caddick, 2018); for the northern Scandian orogenic wedge (i.e., Moine, Ben Hope, Naver, and Skinsdale Thrust; Thigpen et al., 2021) or for generic subduction zones (Peacock, 1992).

6.3. Kinematics of the BT

We define the deformation regime and the finite strain of the BT. The kinematic vorticity data obtained by the C' shear bands method (Kurz and Northrup, 2008), PAR, and the RGN method (Jessup et al., 2007) have allowed quantification of the flow regime as a non-coaxial flow. Concerning the uncertainties in the estimation of the vorticity parameter, all methods, based on different assumptions, return consistent results from both Area I and II. The object lineation within the BT is gently plunging and generally parallel to the dip of the main foliation, and thus is compatible with a thrust-sense movement. Our data highlight that the component of the simple shear

increases progressively towards the centre of the BT, from both HW and FW rocks and in both Area I and II (Fig. 11b). We observe a general variation of simple shear from ~33% up to ~77%. Mylonites and less deformed rocks record a flow regime dominated by pure shear, whereas ultramylonites in the center of the shear zone record an increasing amount of simple shear. This is associated with a change of the finite strain ellipsoid, from close to the plane strain up to prolate conditions.

Our results are in good agreement with the previous work on the BT. In fact, asymmetric F_2 folds observed in both nappes with the axial plane parallel to the mylonitic foliation are linked to the BT non-coaxial deformation (Carosi et al., 2004). According to the description by Fossen (2016), it is possible to suggest that the presence of this kind of fold accommodates the component of shortening perpendicular to the BT. Contemporaneous pure and simple shearing, due to the overthrust of the Internal Nappe Zone onto the External Nappe Zone, may explain the F_2 folds. Finite strain data suggest a variation from general flattening to prolate ellipsoid, in agreement with an increase of simple shear in thrust-sense shear zones (Vitale and Mazzoli, 2008; Fossen, 2016). A higher R_{xz} value is inferred from ultramylonitic/within core samples compared to values from the other mylonitic samples, corroborating both field and microstructural observations. This implies that the core of the BT accommodated a higher amount of strain with respect to the shear zone peripheries (Fossen and Cavalcante, 2017). Higher W_k values, within the centre of the BT, and a prolate strain ellipsoid are associated with higher RSCM T, whereas lower W_k values, far from the BT core, and plane strain conditions are associated with samples showing lower RSCM T.

(insert Figure 11 here)

The progressive increase in temperature towards the BT, coupled with the increase of simple shear, could indicate a syn-shearing temperature imprint. This broad correlation between RSCM T and the deformation gradient could imply that the flow path was accompanied by a progressive localization of deformation in the core of the shear zone, due to thermal weakening, during the ductile deformation (Vitale and Mazzoli, 2008). Although we lack absolute timing constraints, these results fit well with the Type II shear zone growth model proposed by Fossen and Cavalcante (2017). In this case, following the hypothesis of the shear heating model discussed above, the deformation has been progressively localized in the central part of the shear zone due to thermal weakening. The

result, as in the here study case of the BT, is a shear zone with a deformation gradient increasing toward the centre along with, associated to systematic variations in kinematic vorticity, finite strain and T based on RSCM (Fig. 12). (insert Figure 12 here)

7. Conclusions

This study shows the importance of studying regional-scale shear zones with a multidisciplinary approach. We provide quantitative constraints on deformation and peak temperature in two sectors of the BT (Fig. 12). The strictly similar thermo-kinematic results and the same sense of shear obtained from two different sectors along the BT (Area I and Area II) confirm the post-nappe stacking folded structure (i.e., Barbagia Synform) of the belt (Fig. 12). Valuable information can only be obtained if different and independent techniques are integrated to constrain temperature and deformation in terms of peak temperature, finite strain, and kinematics of the flow. Detecting a thermal gradient and, whenever possible, identifying the process that produces heating in a thrust-sense shear zone in collisional systems is one of the primary results of this work. A combination of structural investigations at different scales and of RSCM analyses reveals an increase in finite strain and of the simple shear component coupled with the systematic increase in RSCM T, approaching the high-strain zone from the structurally higher parts of the HW or from the structurally lower parts of the FW (Fig. 12). Regarding the nature of the heating, our thermal results document that the paleothermal architecture of the BT best fits with a tectonic scenario of shear heating. The heating quantified along the BT (~ 50 °C) is in agreement with the shear heating magnitudes calculated by numerical and mechanical studies. By integrating different methodologies, we show that the BT represents a major tectonic boundary that drove exhumation, divides the internal sector of the Sardinian orogenic wedge from the external one, and represents a change from hinterland- to foreland-style deformation.

Acknowledgements

We want to thank Mutsuki Aoya and J. Ryan Thigpen for their constructive and thorough reviews. We thank Fabrizio Agosta for his efficient editorial work. We also want to thank Jacob Forshaw for his useful suggestions.

References

- 479 Aoya, M., Kouketsu, Y., Endo, S., Shimizu, H., Mizukami, T., Nakamura, D., Wallis, S., 2010. Extending the
480 applicability of the Raman carbonaceous-material geothermometer using data from contact metamorphic rocks.
481 *Journal of Metamorphic Geology* 28, 95–914. <https://doi.org/10.1111/j.1525-1314.2010.00896.x>
- 482 Bailey, C.M., Polvi, L.E., Forte, A.M., 2007. Pure shear dominated high-strain zones in basement terranes.
483 *Geological Society American Memories* 200, 93-108.
- 484 Barca, S., Forci, A., Funedda, A., 2003. Nuovi dati stratigrafico-strutturali sul flysch ercinico dell'Unità del Gerrei
485 (Sardegna SE). In: Pascucci, V., (Ed.), *GeoSed*, Alghero 28-30 settembre 2003, 2003, 291–298, Sassari: University
486 of Sassari.
- 487 Bellanger, M., Augier, R., Bellahsen, N., Jolivet, L., Monié, P., Baudin, T., Beyssac, O., 2015. Shortening of the
488 European Dauphinois margin (Oisans Massif, Western Alps): new insights from RSCM maximum temperature
489 estimates and $40\text{Ar}/39\text{Ar}$ in situ dating. *Journal of Geodynamics* 83, 37–64.
490 <https://doi.org/10.1016/j.jog.2014.09.004>
- 491 Behr, W.M., Platt, J.P., 2014. Brittle faults are weak, yet the ductile middle crust is strong: implications for
492 lithospheric mechanics. *Geophysical Research Letters* 41, 8067-8075.
- 493 Beyssac, O., Lazzeri, M., 2012. Application of Raman spectroscopy to the study of graphitic carbons in the Earth
494 Sciences. In: Dubessy, J., Caumon, M.-C., Rull, F., *Raman spectroscopy applied to Earth sciences and cultural*
495 *heritage*, Mineralogical Society of Great Britain and Ireland 12, 415–454. [http://dx.doi.org/10.1180/emu-](http://dx.doi.org/10.1180/emu-notes.12.12)
496 [notes.12.12](http://dx.doi.org/10.1180/emu-notes.12.12)
- 497 Beyssac, O., Goffé, B., Chopin, C., Rouzaud, J. N., 2002. Raman spectra of carbonaceous material in
498 metasediments: a new geothermometer. *Journal of Metamorphic Geology* 20(9), 859–871.
499 <https://doi.org/10.1046/j.1525-1314.2002.00408.x>
- 500 Beyssac, O., Goffé, B., Petitot, J.-P., Froigneux, E., Moreau, M., Rouzaud, J.-N., 2003. On the characterization of
501 disordered and heterogeneous carbonaceous materials by Raman spectroscopy. *Spectrochimica Acta A* 59(10),
502 2267–2276. [https://doi.org/10.1016/S1386-1425\(03\)00070-2](https://doi.org/10.1016/S1386-1425(03)00070-2)
- 503 Beyssac, O., Bollinger, L., Avouac, J.P. Goffé, B., 2004. Thermal metamorphism in the lesser Himalaya of Nepal
504 determined from Raman spectroscopy of carbonaceous material. *Earth and Planetary Science Letters* 225, 233–
505 241. <https://doi.org/10.1016/j.epsl.2004.05.023>
- 506 Beyssac, O., Pattison, D.R.M., Bourdelle, F., 2019. Contrasting degrees of recrystallization of carbonaceous
507 material in the Nelson aureole, British Columbia and Ballachulish aureole, Scotland, with implications for
508 thermometry based on Raman spectroscopy of carbonaceous material. *Journal of Metamorphic Geology* 37, 71–
509 95. <https://doi.org/10.1111/jmg.12449>

- 510 Berger, A., Engi, M., Erne-Schmid, S., Glotzbach, C., Spiegel, C., de Goede, R., Herwegh, M., 2020. The relation
511 between peak metamorphic temperatures and subsequent cooling during continent–continent collision (western
512 Central Alps, Switzerland). *Swiss Journal of Geosciences* 113, 4. <https://doi.org/10.1186/s00015-020-00356-4>
- 513 Bollinger, L., Avouac, J. P., Beyssac, O., Catlos, E. J., Harrison, T. M., Grove, M., Goffé, B., Sapkota, S., 2004.
514 Thermal structure and exhumation history of the Lesser Himalaya in central Nepal. *Tectonics* 23(5), TC2015.
515 <https://doi.org/10.1029/2003TC001564>
- 516 Brown, M., 1993. P-T-t evolution of orogenic belts and the causes of regional metamorphism. *Journal of the*
517 *Geological Society* 150, 227–241.
- 518 Brun, J.-P., Cobbold, P.R., 1980. Strain heating and thermal softening in continental shear zones: a review. *Journal*
519 *of Structural Geology* 2, 149-158.
- 520 Burg, J.-P., Gerya, T.-V., 2005. The role of viscous heating in Barrovian metamorphism of collisional orogens:
521 Thermomechanical models and application to the Lepontine Dome in the Central Alps. *Journal of Metamorphic*
522 *Geology* 23, 75–95. <https://doi.org/10.1111/j.1525-1314.2005.00563.x>
- 523 Burg, J.-P., Schmalholz, S., 2008. Viscous heating allows thrusting to overcome crustalscale buckling: numerical
524 investigation with application to the Himalayan syntaxes. *Earth and Planetary Science Letters* 274 (1–2), 189–203.
525 <https://doi.org/10.1016/j.epsl.2008.07.022>
- 526 Calvino, F., 1959. Lineamenti strutturali del Sarrabus-Gerrei (Sardegna sud-orientale). *Bollettino del Servizio*
527 *Geologico d'Italia* 81(4–5), 489–556.
- 528 Camacho, A., McDougall, I., Armstrong, R., Braun, J., 2001. Evidence for shear heating, Musgrave Block, central
529 Australia. *Journal of Structural Geology* 23, 1007-1013.
- 530 Carmignani, L., Minzoni, N., Pertusati, P.C., Gattiglio, M., 1982. Lineamenti geologici principali del Sarcidano-
531 Barbagia di Belvì. In: Carmignani, L., Cocozza, T., Ghezzi, C., Pertusati, P.C., Ricci, C.A. (Ed.), *Guida alla*
532 *Geologia del Paleozoico Sardo. Guide Geologiche Regionali, Società Geologica Italiana*, 119–125.
- 533 Carmignani, L., Carosi, R., Di Pisa, A., Gattiglio, M., Musumeci, G., Oggiano, G., Pertusati, P.C., 1994. The
534 hercynian chain in Sardinia (Italy). *Geodinamica Acta* 7(1), 31–47.
535 <https://doi.org/10.1080/09853111.1994.11105257>
- 536 Carmignani, L., Oggiano, G., Barca, S., Conti, P., Eltrudis, A., Funedda, A., Pasci, S., Salvadori, I., 2001. *Geologia*
537 *della Sardegna (Note illustrative della Carta Geologica della Sardegna in scala 1:200.000). Memorie descrittive*
538 *della Carta Geologica d'Italia, Servizio Geologico Nazionale, Istituto Poligrafico e Zecca dello Stato, Roma.*

- 539 Carmignani, L., Oggiano, G., Funedda, A., Conti, P., Pasci, S., 2015. The geological map of Sardinia (Italy) at
540 1:250,000 scale. *Journal of Maps* 12(5), 826–835. <https://doi.org/10.1080/17445647.2015.1084544>
- 541 Carosi R., 2004. Carta geologico-strutturale del Monte S. Vittoria (Sarcidano-Barbagia di Belvi, Sardegna centrale,
542 Italia). Carosi, R., Elter, F.M., Gattiglio, M. (1997). Scala 1:25.000, Centrooffset, Siena, 1997. *Atti della Società*
543 *Toscana di Scienze Naturali serie A* 108 (2002-2003).
- 544 Carosi, R., Malfatti, G., 1995. Analisi Strutturale dell'Unità di Meana Sardo e caratteri della deformazione duttile
545 nel Sarcidano-Barbagia di Seulo (Sardegna centrale, Italia). *Atti della Società Toscana di Scienze Naturali, Serie*
546 *A* 102, 121–136.
- 547 Carosi, R., Pertusati, P.C., 1990. Evoluzione strutturale delle unità tettoniche erciniche nella Sardegna centro-
548 meridionale. *Bollettino della Società Geologica Italiana* 109, 325–335.
- 549 Carosi, R., Iacopini, D., Montomoli, C., 2004. Asymmetric folds development in the Variscan Nappe of central
550 Sardinia (Italy). *Comptes Rendus Geoscience* 336(10), 939–949. <https://doi.org/10.1016/j.crte.2004.03.004>
- 551 Carosi, R., Leoni, L., Paolucci, F., Pertusati, P.C., Trumpy, E., 2010. Deformation and illite crystallinity in
552 metapelitic rocks from the Mandas area, in the Nappe Zone of the Variscan belt of Sardinia; *Rendiconti Online*
553 *Società Geologica Italiana* 11, 393–394.
- 554 Carosi, R., Montomoli, C., Iacopini, D., 2002. Le pieghe asimmetriche dell'Unità di Meana Sardo, Sardegna
555 centrale (Italia): evoluzione e meccanismi di piegamento. *Atti della Società Toscana di Scienze Naturali, Serie A*
556 108, 51–58.
- 557 Carosi, R.; Montomoli, C.; Tiepolo, M.; Frassi, C. Geochronological constraints on post-collisional shear zones in
558 the Variscides of Sardinia (Italy). *Terra Nov.* 2012, 24, 42–51. <https://doi.org/10.1111/j.1365-3121.2011.01035.x>
- 559 Carosi, R., Musumeci, G., Pertusati, P.C., 1991. Differences in the structural evolution of tectonic units in central-
560 southern Sardinia. *Bollettino della Società Geologica Italiana* 110(3-4), 543–551.
- 561 Carosi, R., Petroccia, A., Iaccarino, S., Simonetti, M., Langone, A., Montomoli, C., 2020. Kinematics and timing
562 constraints in a transpressive tectonic regime: the example of the Posada-Asinara shear zone (NE Sardinia, Italy).
563 *Geosciences* 10, 288. <https://doi.org/10.3390/geosciences10080288>
- 564 Casini, L., Cuccuru, S., Maino, M., Oggiano, G., Tiepolo, M., 2012. Emplacement of the Arzachena Pluton
565 (Corsica-Sardinia Batholith) and the geodynamics of incoming Pangaea. *Tectonophysics* 544–545, 31–49.
566 <https://doi.org/10.1016/j.tecto.2012.03.028>
- 567 Casini, L., Funedda, A., Oggiano, G., 2010. A balanced foreland-hinterland deformation model for the Southern
568 Variscan belt of Sardinia, Italy. *Geological Journal* 45(5-6), 634–649. <https://doi.org/10.1002/gj.1208>

- Chen, C.-T., Chan, Y.-C., Lu, C.-Y., Simoes, M., Beyssac, O., 2011. Nappe structure revealed by thermal constraints in the Taiwan metamorphic belt. *Terra Nova* 23, 85-91. <https://doi.org/10.1111/j.1365-3121.2011.00987.x>
- Cocco, F., Funedda, A., 2011. New data on the pre-Middle Ordovician deformation in SE Sardinia: a preliminary note. *Rendiconti online della Società Geologica Italiana* 15, 34–36.
- Cocco, F., Funedda, A., 2017. The Sardic phase: field evidence of Ordovician tectonics in SE Sardinia, Italy. *Geological Magazine*, 1–14, <https://doi.org/10.1017/s0016756817000723>
- Cocco, F., Oggiano, G., Funedda, A., Loi, A., Casini, L., 2018. Stratigraphic, magmatic and structural features of Ordovician tectonics in Sardinia (Italy): a review. *Journal of Iberian Geology* 44, 619–639. <https://doi.org/10.1007/s41513-018-0075-1>
- Conti, P., Patta, E., 1998. Large scale Hercynian W-directed tectonics in southeastern Sardinia (Italy). *Geodinamica Acta* 11(5), 217–231.
- Conti, P., Funedda, A., Cerbai, N., 1998. Mylonite development in the Hercynian basement of Sardinia (Italy). *Journal of Structural Geology* 20(2/3), 121–133. [https://doi.org/10.1016/S0191-8141\(97\)00091-6](https://doi.org/10.1016/S0191-8141(97)00091-6)
- Conti, P., Carmignani, L., Cerbai, N., Eltrudis, A., Funedda, A., Oggiano, G., 1999. From thickening to extension in the Variscan belt - kinematic evidence from Sardinia (Italy). *Terra Nova* 11(2/3), 93–99, <https://doi.org/10.1046/j.1365-3121.1999.00231.x>
- Conti, P., Carmignani, L., Funedda, A., 2001. Change of nappe transport direction during the Variscan collisional evolution of central-southern Sardinia (Italy). *Tectonophysics* 332(1–2), 255–273, [https://doi.org/10.1016/S0040-1951\(00\)00260-2](https://doi.org/10.1016/S0040-1951(00)00260-2)
- Coward, M.P., Kim, J.H., 1981. Strain within thrust sheets. In: McClay, K.R., Price, N.J. (Eds.), *Thrust and Nappe Tectonics*. Geological Society of London Special Publication 9, 275-292.
- Cruciani, G., Montomoli, C., Carosi, R., Franceschelli, M., Puxeddu, M., 2015. Continental collision from two perspectives: a review of Variscan metamorphism and deformation in northern Sardinia. *Periodico di Mineralogia* 84, 3B, 657–699.
- Dahlen, F.A., Suppe, J., Davis, D., 1984. Mechanics of fold-and-thrust belts and accretionary wedges — cohesive Coulomb theory. *Journal of Geophysical Research* 89, 87–101.
- Del Moro, A., Di Simplicio, P., Ghezzi, C., Guasparri, G., Rita, F., Sabatini, G., 1975. Radiometric data and intrusive sequence in the Sardinian batholith. *Neues Jahrbuch für Mineralogie Monatshefte* 126, 28–44.

- 598 Delchini, S., Lahfid, A., Plunder, A., Michard, A., 2016. Applicability of the RSCM geothermometry approach in
599 a complex tectono-metamorphic context: The Jebilet massif case study (Variscan Belt, Morocco). *Lithos* 256–257,
600 1–12. <https://doi.org/10.1016/j.lithos.2016.04.007>
- 601 Dessau, G., Duchi, G., Moretti, A., Oggiano, G., 1982. Geologia della zona del Valico di Correboi (Sardegna
602 centro-orientale). Rilevamento, tettonica e giacimenti minerari. *Bollettino della Società Geologica Italiana* 101,
603 223–231.
- 604 Di Vincenzo, G., Carosi, R., Palmeri, R., 2004. The relationship between tectono-metamorphic evolution and
605 argon isotope records in white mica: Constraints from in situ ^{40}Ar - ^{39}Ar laser analysis of the Variscan basement
606 of Sardinia. *Journal of Petrology* 45, 1013–1043. <https://doi.org/10.1093/petrology/egh002>
- 607 Duretz, T., Schmalholz, S., Podladchikov, Y., Yuen, D., 2014. Physics-controlled thickness of shear zones caused
608 by viscous heating: implications for crustal shear localization. *Geophysical Research Letters* 41 (14), 4904–4911
- 609 Elliott, D., 1976. Motion of thrust sheets. *Geophysical Research Letters* 81, 949–963.
- 610 Fauconnier, J., Labrousse, L., Andersen, T.B., Beyssac, O., Duprat-Oualid, S., Yamato, P., 2014. Thermal
611 structure of a major crustal shear zone, the basal thrust in the Scandinavian Caledonides, *Earth and Planetary*
612 *Science Letters* 385, 162–171. <https://doi.org/10.1016/j.epsl.2013.10.038>
- 613 Ferreiro Mählmann, R., Bozkaya, Ö., Potel, S., Le Bayon, R., Šegvić, B., Nieto, F., 2012. The pioneer work of
614 Bernard Kübler and Martin Frey in very low-grade metamorphic terranes: paleo-geothermal potential of variation
615 in Kübler-index/organic matter reflectance correlations. A review. *Swiss Journal of Geosciences* 105, 121–152.
- 616 Flinn, D., 1962. On folding during three-dimensional progressive deformation. *The Quarterly journal of the*
617 *Geological Society of London* 118, 385–433
- 618 Fossen, H., 2016. *Structural Geology*, second ed. Cambridge University Press, Cambridge, United Kingdom.
- 619 Fossen, H., Cavalcante, G.C.G., 2017. Shear zones – a review. *Earth-Science Reviews* 171, 434–455.
620 <https://doi.org/10.1016/j.earscirev.2017.05.002>
- 621 Franceschelli, M., Gattiglio, M., Pannuti, F., Fadda, S., 1992. Illite crystallinity in pelitic rocks from the external
622 and nappe zones of the Hercynian chain of Sardinia. In: Carmignani, L., Sassi, F.P., (Ed.), *Contributions to the*
623 *Geology of Italy with special regard to the Paleozoic Basements: IGCP Project No. 276, Newsletter* 127–135.
- 624 Franceschelli, M., Puxeddu, M., Cruciani, G., 2005. Variscan metamorphism in Sardinia, Italy: review and
625 discussion. *Journal of the Virtual Explorer* 19, 2. <http://dx.doi.org/10.3809%2Fjvirtex.2005.00121>
- 626 Fry, N., 1979. Random point distribution and strain measurement in rocks. *Tectonophysics* 60, 89–105.
627 [https://doi.org/10.1016/0040-1951\(79\)90135-5](https://doi.org/10.1016/0040-1951(79)90135-5)

- Funedda, A., 2009. Foreland- and hinterland-verging structures in fold-and-thrust belt: an example from the Variscan foreland of Sardinia. *International Journal of Earth Sciences* 98, 1625–1642, <https://doi.org/10.1007/s00531-008-0327-y>
- Funedda, A., Naitza, S., Conti, P., Dini, A., Butta, C., Tocco, S., Carmignani, L., 2011. The geological and metallogenic map of the Baccu Locci mine area (Sardinia, Italy). *Journal of Maps* 7(1), 103–114. <https://doi.org/10.4113/jom.2011.1134>
- Funedda, A., Meloni, M.A., Loi, A., 2015. Geology of the Variscan basement of the Laconi-Asuni area (central Sardinia, Italy): the core of a regional antiform refolding a tectonic nappe stack. *Journal of Maps* 11(1), 146–156. <https://doi.org/10.1080/17445647.2014.942396>
- Furuichi, H., Ujiie, K., Kouketsu, Y., Saito, T., Tsutsumi, A., Wallis, S., 2015. Vitrinite reflectance and Raman spectra of carbonaceous material as indicators of frictional heating on faults: Constraints from friction experiments. *Earth and Planetary Science Letters* 424, 191–200. <https://doi.org/10.1016/j.epsl.2015.05.037>
- Galy, V., Beyssac, O., France-Lanord, C., and Eglinton, T. I., 2008 Recycling of graphite during Himalayan erosion: A geological stabilization of carbon in the crust. *Science* 322, 943–945 <http://dx.doi.org/10.1126/science.1161408>
- Ghosh, P., Bhattacharyya, K., Parui, C., 2020. Tracking progressive deformation of an orogenic wedge through two successive internal thrusts: Insights from structure, deformation profile, strain, and vorticity of the Main Central thrust (MCT) and the Pelling-Munsiari thrust (PT), Sikkim Himalayan fold thrust belt. *Journal of Structural Geology* 140. <https://doi.org/10.1016/j.jsg.2020.104120>
- Gillam, B.G., Little, T.A., Smith, E., Toy V.G., 2013. Extensional shear band development on the outer margin of the Alpine mylonite zone, Tattare Stream, Southern Alps, New Zealand. *Journal of Structural Geology* 54, 1–20. <https://doi.org/10.1016/j.jsg.2013.06.010>
- Grasemann, B., Fritz, H., Vannay, J.C., 1999. Quantitative kinematic flow analysis from the Main Central Thrust Zone (NW-Himalaya, India): implications for a decelerating strain path and the extrusion of orogenic wedges. *Journal of Structural Geology* 21, 837–853. [https://doi.org/10.1016/s0191-8141\(99\)00077-2](https://doi.org/10.1016/s0191-8141(99)00077-2)
- Grujic, D., Ashley, K. T., Coble, M. A., Coutand, I., Kellett, D. A., Larson, K. P., Whipp, D. M. Jr., Gao, M., Whynot, N., 2020. Deformational temperatures across the Lesser Himalayan Sequence in eastern Bhutan and their implications for the deformation history of the Main Central Thrust. *Tectonics* 39, e2019TC005914. <https://doi.org/10.1029/2019TC005914>

- Handy, M., Hirth, G., Bürgmann, R., 2007. Continental fault structure and rheology from the frictional-to-viscous transition downward. In: Handy, M., Hirth, G., Hovius, N. (Ed.), *Tectonic Faults: Agents of Change on a Dynamic Earth*. The MIT Press., Cambridge, Mass.
- Henry, D.G., Jarvis, I., Gillmore, G., Stephenson, M., 2019. Raman spectroscopy as a tool to determine the thermal maturity of organic matter: Application to sedimentary, metamorphic and structural geology. *Earth-Science Reviews* 198, 102936. <https://doi.org/10.1016/j.earscirev.2019.102936>
- Hirth, G., Teyssier, C., Dunlap, W.J., 2001. An evaluation of quartzite flow laws based on comparisons between experimentally and naturally deformed rocks. *International Journal of Earth Sciences* 90, 77–87
- Iaccarino, S., Montomoli, C., Montemagni, C., Massonne, H. –J., Langone, A., Jain, A. K., Visona, D., Carosi, R., 2020. The main central thrust zone along the Alaknanda and Dhaul Ganga valleys (Garhwal Himalaya, NW India): Insights into an inverted metamorphic sequence. *Lithos* 372–373, 105669. <https://doi.org/10.1016/j.lithos.2020.105669>
- Iacopini, D., Frassi, C., Carosi, R., Montomoli, C., 2011. Biases in three-dimensional vorticity analysis using porphyroclast system: Limits and application to natural examples. *Geological Society of London, Special Publications* 360, 301–318. <https://doi.org/10.1144/SP360.17>
- Jaboyedoff, M., Bussy, F., Kübler, B., Thelin, P., 2001. Illite “crystallinity” revisited. *Clay Minerals* 49, 156–167.
- Jamieson, R.A., Beaumont, C., 2013. On the origin of orogens. *Geological Society of America Bulletin* 125, 1671–1702. <https://doi.org/10.1130/B30855.1>
- Jaquet, Y., Duretz, T., Grujic, D., Masson, H., Schmalholz, S. M., 2018. Formation of orogenic wedges and crustal shear zones by thermal softening, associated topographic evolution and application to natural orogens. *Tectonophysics* 746, 512–529. <https://doi.org/10.1016/j.tecto.2017.07.021>
- Jessup, M. J., Law, R. J., Frassi, C., 2007. The Rigid Grain Net (RGN): An alternative method for estimating mean kinematic vorticity number (Wm). *Journal of Structural Geology* 29, 411–421. <https://doi.org/10.1016/j.jsg.2006.11.003>
- Kaneki, S., Hirono, T., Mukoyoshi, H., Sampei, Y., Ikehara, M., 2016. Organochemical characteristics of carbonaceous materials as indicators of heat recorded on an ancient plate-subduction fault, *Geochemistry, Geochemistry, Geophysics, Geosystems* 17(7), 2855–2868, [doi:10.1002/2016GC006368](https://doi.org/10.1002/2016GC006368)
- Kedar, L., Bond, C., Muirhead, D., 2020. Carbon ordering in an aseismic shear zone: implications for crustal weakening and Raman spectroscopy. *EGU General Assembly 2020, Online*, 4–8 May 2020, EGU2020-9155. <https://doi.org/10.5194/egusphere-egu2020-9155>

- 687 Kitamura, M., Mukoyoshi, H., Fulton, P.M., Hirose, T., 2012. Coal maturation by frictional heat during rapid
688 fault slip. *Geophysical Research Letters* 39, 1–5. <https://doi.org/10.1029/2012gl052316>
- 689 Kouketsu, Y., Miyake, A., Igami, Y., Taguchi, T., Kagi, H., Enami, M., 2019. Drastic effect of shearing on graphite
690 microtexture: attention and application to Earth science. *Prog. Earth and Planetary Science Letters* 6, 23.
691 <https://doi.org/10.1186/s40645-019-0271-4>
- 692 Kouketsu, Y., Mizukami, T., Mori, H., Endo, S., Aoya, M., Hara, H., Nakamura, D., Wallis, S., 2014. Raman CM
693 geothermometer using FWHM. *Island Arc* 23, 33–50. <https://doi.org/10.1111/iar.12057>
- 694 Kříbek, B., Sýkorová, I., Machovič, V., Laufek, F., 2008. Graphitization of organic matter and fluid-deposited
695 graphite in Palaeoproterozoic (Birimian) black shales of the Kaya-Goren greenstone belt (Burkina Faso, West
696 Africa). *Journal of Metamorphic Geology* 26, 937–958. <https://doi.org/10.1111/j.1525-1314.2008.00796.x>
- 697 Kuo, L.-W., Di Felice, F., Spagnuolo, E., Di Toro, G., Song, S.-R., Aretusini, S., Li, H., Suppe, J., Si, J., Wen, C.-
698 Y., 2017 Fault gouge graphitization as evidence of past seismic slip. *Geology* 45 (11), 979–982.
699 <https://doi.org/10.1130/G39295.1>
- 700 Kuo L.W., Huang, J.R., Fang, J.N., Si, J., Song, S.R., Li, H., Yeh, E.C., 2018. Carbonaceous materials in the fault
701 zone of the longmenshan fault belt: 2. characterization of fault gouge from deep drilling and implications for fault
702 maturity. *Minerals* 8(9), 393. <https://doi.org/10.3390/min8100457>
- 703 Kurz, G.A., Northrup, C.J., 2008. Structural analysis of mylonitic fault rocks in the Cougar Creek Complex,
704 Oregon-Idaho using the porphyroclast hyperbolic distribution method, and potential use of sc'-type extensional
705 shear bands as quantitative vorticity indicators. *Journal of Structural Geology* 30, 1005–1012.
706 <https://doi.org/10.1016/j.jsg.2008.04.003>
- 707 Lahfid, A., Beyssac, O., Deville, E., Negro, F., Chopin, C., Goffé, B., 2010. Evolution of the Raman spectrum of
708 carbonaceous material in low-grade metasediments of the Glarus Alps (Switzerland). *Terra Nova* 22, 354–360.
709 <https://doi.org/10.1111/j.1365-3121.2010.00956.x>
- 710 Larson, K. P., Godin, L., Davis, W. J., Davis, D. W., 2010. Relationships between displacement and distortion in
711 orogens: Linking the Himalayan foreland and hinterland in central Nepal. *Geological Society of America Bulletin*
712 122, 1116–1134. <https://doi.org/10.1130/b30073.1>
- 713 Law, R.D., 2014. Deformation thermometry based on quartz c-axis fabrics and recrystallization microstructures:
714 A review. *Journal of Structural Geology* 66, 129–161. <https://doi.org/10.1016/j.jsg.2014.05.023>

- 715 Law, R.D., Searle, M.P., Simpson, R.L., 2004. Strain, deformation temperatures and vorticity of flow at the top of
 716 the Greater Himalayan Slab, Everest Massif, Tibet. *Journal of the Geological Society* 161, 305–320.
 717 <https://doi.org/10.1144/0016-764903-047>
- 718 Law, R.D., Thigpen, J.R., Mazza, S.E., Mako, C.A., Krabbendam, M., Spencer, B.M., Ashley, K.T., Strachan,
 719 R.A., Davis, E.F., 2021. Tectonic Transport Directions, Shear Senses and Deformation Temperatures Indicated by
 720 Quartz c-Axis Fabrics and Microstructures in a NW-SE Transect across the Moine and Sgurr Beag Thrust Sheets,
 721 Caledonian Orogen of Northern Scotland. *Geosciences* 11, 411. <https://doi.org/10.3390/geosciences11100411>
- 722 Lyu, M., Cao, S., Neubauer, F., Xuemei Cheng, J.L., 2020. Deformation fabrics and strain localization mechanisms
 723 in graphitic carbon-bearing rocks from the Ailaoshan-Red River strike-slip fault zone. *Journal of Structural*
 724 *Geology* 140. <https://doi.org/10.1016/j.jsg.2020.104150>
- 725 Maino, M., Casini, L., Ceriani, A., Decarlis, A., Di Giulio, A., Seno, S., Setti, M., Stuart, F., 2015. Dating shallow
 726 thrusts with zircon (U-Th)/ He thermochronometry - The shear heating connection. *Geology* 43(6), 495-498.
 727 <https://doi.org/10.1130/G36492.1>
- 728 Mako, C.A., Caddick, M.J., 2018. Quantifying magnitudes of shear heating in metamorphic systems.
 729 *Tectonophysics* 744, 499–517. <https://doi.org/10.1016/j.tecto.2018.07.003>
- 730 Malavieille, J., Dominguez, S., Lu, C.-Y., Chen, C.-T., Konstantinovskaya, E., 2019. Deformation partitioning in
 731 mountain belts: insights from analogue modelling experiments and the Taiwan collisional orogen. *Geological*
 732 *Magazine* 158(1), 1-20. <https://doi.org/10.1017/S0016756819000645>
- 733 Matte, P., 2001. The Variscan collage and orogeny (480–290 ma) and the tectonic definition of the Armorica
 734 microplate: A review. *Terra Nova* 13, 117–121. <https://doi.org/10.1046/j.1365-3121.2001.00327.x>
- 735 Merriman, R.J., Roberts, B., Peacor, D.R., Hirons, S.R., 1995. Strain-related differences in the crystal growth of
 736 white mica and chlorite: a TEM and XRD study of development of pelite microfabrics in the Southern Uplands
 737 thrust terrane, Scotland. *Journal of Metamorphic Geology* 13, 559-576.
- 738 Mitra, G., 1994. Strain variation in thrust sheets across the Sevier fold-and-thrust belt (Idaho- Utah-Wyoming):
 739 implications for section restoration and wedge taper evolution. *Journal of Structural Geology* 16, 585-602.
- 740 Molli, G., Vitale Brovarone, A., Beyssac, O., Cinquini, I., 2018. RSCM thermometry in the Alpi Apuane (NW
 741 Tuscany, Italy): New constraints for the metamorphic and tectonic history of the inner northern Apennines. *Journal*
 742 *of Structural Geology* 113, 200–216. <https://doi.org/10.1016/j.jsg.2018.05.020>.
- 743 Molnar, P., England, P., 1990. Temperatures, heat flux, and frictional stress near major thrust faults. *Journal of*
 744 *Geophysical Research* 95, 4833. <https://doi.org/10.1029/JB095iB04p04833>.

- 745 Montési, L.G.J., 2013. Fabric development as the key for forming ductile shear zones and enabling plate tectonics.
 746 *Journal of Structural Geology* 50, 254–266. <https://doi.org/10.1016/j.jsg.2012.12.011>
- 747 Montési, L.G.J., Zuber, M.T., 2002. A unified description of localization for application to large-scale tectonics.
 748 *Journal of Geophysical Research* 107 (B3), 1–21. <https://doi.org/10.1029/2001JB000465>
- 749 Montmartin, C., Faure, M., Raimbourg, H., 2021. Paleotemperature investigation of the Variscan southern external
 750 domain: the case of the Montagne Noire (France). *BSGF - Earth Sciences Bulletin* 192 :3
 751 <http://dx.doi.org/10.1051/bsgf/2020043>
- 752 Montomoli, C., 2003. Zone di taglio fragili-duttili nel basamento varisco metamorfico di basso grado della Nurra
 753 meridionale (Sardegna nord-occidentale). *Atti della Società Toscana di Scienze Naturali, Serie A* 108, 23–29.
- 754 Montomoli, C., Iaccarino, S., Simonetti, M., Lezzerini, M., Carosi, R., 2018. Structural setting, kinematics and
 755 metamorphism in a km-scale shear zone in the inner nappes of Sardinia (Italy). *Italian Journal of Geosciences* 137,
 756 294–310. <https://doi.org/10.3301/IJG.2018.16>
- 757 Mori, H., Mori, N., Wallis, S., Westaway, R., Annen, C., 2017. The importance of heating duration for Raman
 758 CM thermometry: evidence from contact metamorphism around the Great Whin Sill intrusion, UK. *Journal of*
 759 *Metamorphic Geology* 35, 165–180. <https://doi.org/10.1111/jmg.12225>
- 760 Moris-Muttoni, B., Raimbourg, H., Augier, R., Champallier, R., LeTrong, E., 2022. The impact of melt versus
 761 mechanical wear on the formation of pseudotachylite veins in accretionary complexes. *Scientific Reports* 12,
 762 1529. <https://doi.org/10.1038/s41598-022-05379-5>
- 763 Muirhead, D. K., Kedar, L., Schito, A., Corrado, S., Bond, C. E., Romano, C., 2021. Raman spectral shifts in
 764 naturally faulted rocks. *Geochemistry, Geophysics, Geosystems*, 22, e2021GC009923.
 765 <https://doi.org/10.1029/2021GC009923>
- 766 Musumeci, G., 1992. Ductile wrench tectonics and exhumation of hercynian metamorphic basement in Sardinia:
 767 Monte Grighini Complex. *Geodinamica Acta* 5(1-2), 119–133
- 768 Nakamura, Y., Ohashi, K., Toyoshima, T., Satish-Kumar, M., Akai, J., 2015. Strain-induced amorphization of
 769 graphite in fault zones of the Hidaka metamorphic belt, Hokkaido, Japan. *Journal of Structural Geology* 72, 142–
 770 161. <https://doi.org/10.1016/j.jsg.2014.10.012>
- 771 Nakamura, Y., Yoshino, T., Satish-Kumar, M., 2017. An experimental kinetic study on the structural evolution of
 772 natural carbonaceous material to graphite. *American Mineralogist* 102, 135–148. [https://doi.org/10.2138/am-](https://doi.org/10.2138/am-2017-5733)
 773 [2017-5733](https://doi.org/10.2138/am-2017-5733)

- 774 Nakamura, Y., Yoshino, T., Satish-Kumar, M., 2020. Pressure dependence of graphitization: implications for rapid
 775 recrystallization of carbonaceous material in a subduction zone. *Contributions to Mineralogy and Petrology* 175,
 776 32. <https://doi.org/10.1007/s00410-020-1667-2>
- 777 Nibourel, L., Berger, A., Egli, D., Heuberger, S., Herwegh, M., 2021. Structural and thermal evolution of the
 778 eastern Aar Massif: insights from structural field work and Raman thermometry. *Swiss Journal of Geosciences*
 779 114, 9. <https://doi.org/10.1186/s00015-020-00381-3>
- 780 Passchier, C.W., 1987. Stable positions of rigid objects in non-coaxial flow—a study in vorticity analysis. *Journal*
 781 *of Structural Geology* 9, 679 – 690. [https://doi.org/10.1016/0191-8141\(87\)90152-0](https://doi.org/10.1016/0191-8141(87)90152-0)
- 782 Passchier, C.W., Trouw, R. A. J., 2005. *Microtectonics*. Springer, Berlin, Heidelberg. [https://doi.org/10.1007/3-](https://doi.org/10.1007/3-540-29359-0)
 783 [540-29359-0](https://doi.org/10.1007/3-540-29359-0)
- 784 Pavanetto, P., Funedda, A., Northrup, C.J., Schmitz, M., Crowley, J., Loi, A., 2012. Structure and U-Pb zircon
 785 geochronology in the Variscan foreland of SW Sardinia, Italy. *Geological Journal* 47(4), 426–455.
 786 <http://dx.doi.org/10.1002%2Fgj.1350>
- 787 Peacock, S.M., 1992. Blueschist-facies metamorphism, shear heating, and P-T-t paths in subduction shear zones.
 788 *Journal of Geophysical Research* 97.
- 789 Perez-Caceres, I., Martinez Poyatos, D.J., Vidal, O., Beyssac, O., Nieto, F., Simancas, J.F., Azor, A., Bourdelle,
 790 F., 2020. Deciphering the Metamorphic Evolution of the Pulo Do Lobo Metasedimentary Domain (SW Iberian
 791 Variscides). *Solid Earth* 11, 469–488. <https://doi.org/10.5194/se-11-469-2020>
- 792 Pertusati, P., Sarria, E., Cherchi, G.P., Carmignani, L., Barca, S., Benedetti, M., Chighine, G., Cincotti, F.,
 793 Oggiano, G., Ulzega, A., Orrù, P., Pintus, C., 2002. Note illustrative della Carta Geologica d'Italia alla scala
 794 1:50.000 - foglio 541 Jerzu, pp. 143, Servizio Geologico D'Italia.
- 795 Piazzolo, S., Passchier, C.W., 2002. Controls on lineation development in low to medium grade shear zones: a study
 796 from the Cap de Creus peninsula, NE Spain. *Journal of Structural Geology* 24(1), 25–44.
 797 [https://doi.org/10.1016/S0191-8141\(01\)00045-1](https://doi.org/10.1016/S0191-8141(01)00045-1)
- 798 Platt, J.P., 1986. Dynamics of orogenic wedges and the uplift of high-pressure metamorphic rocks. *Geological*
 799 *Society of America Bulletin* 97 (9), 1037–1053.
- 800 Platt, J., 1993. Exhumation of high-pressure rocks: a review of concepts and processes. *Terra Nova* 5 (2), 119–
 801 133.
- 802 Platt, J.P., 2015. Rheology of two-phase systems: a microphysical and observational approach. *Journal of*
 803 *Structural Geology* 77, 213–227.

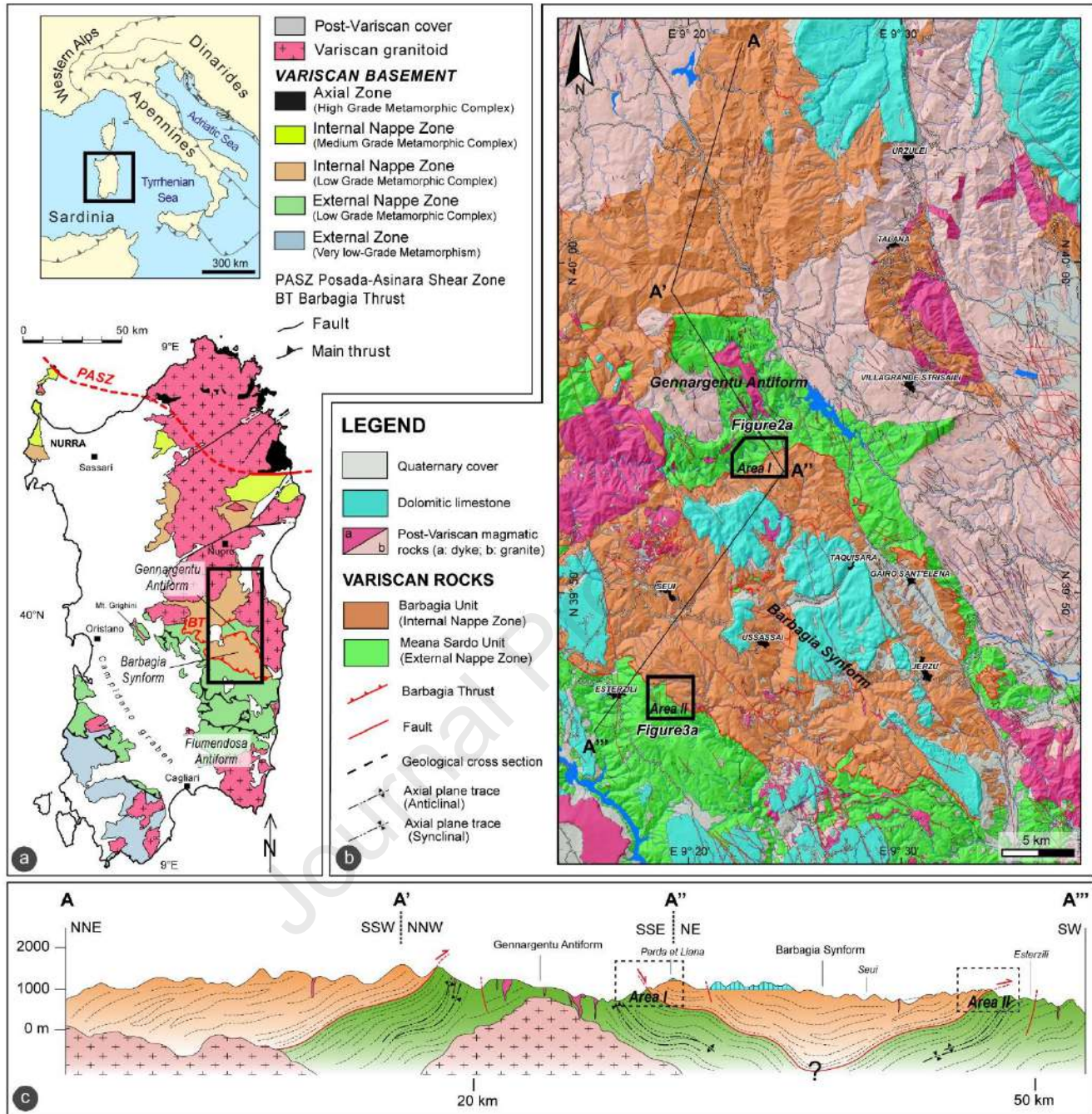
- 804 Platt, J.P., 2018. Corrigendum to “Influence of shear heating on microstructurally defined plate boundary shear
805 zones” [2015, *Journal of Structural Geology*, 79, 80-89]. *Journal of Structural Geology* 113, 242–243.
806 <https://doi.org/10.1016/j.jsg.2017.08.005>
- 807 Platt, J.P., Behr, W.M., 2011. Grainsize evolution in ductile shear zones: Implications for strain localization and
808 the strength of the lithosphere. *Journal of Structural Geology* 33, 537e550.
809 <http://dx.doi.org/10.1016/j.jsg.2011.01.018>
- 810 Platt, J.P., Vissers, R.L.M., 1980. Extensional structures in anisotropic rocks. *Journal of Structural Geology* 2,
811 397–410
- 812 Pryer, L.L., 1993. Microstructures in feldspars from a major crustal thrust zone: The Greenville Front, Ontario,
813 Canada. *Journal of Structural Geology* 15, 21–36. [https://doi.org/10.1016/0191-8141\(93\)90076-M](https://doi.org/10.1016/0191-8141(93)90076-M)
- 814 Ramsay, J. G., 1967. *Folding and fracturing of rocks* McGraw-Hill.
- 815 Rahl, J.M., Anderson, K.M., Brandon, M.T., Fassoulas, C., 2005. Raman spectroscopic carbonaceous material
816 thermometry of lowgrade metamorphic rocks: Calibration and application to tectonic exhumation in Crete, Greece.
817 *Earth and Planetary Science Letters* 240, 339–354. <https://doi.org/10.1016/j.epsl.2005.09.055>
- 818 Rantitsch, G., Iglseder, C., Schuster, R., Hollinetz, M. S., Huet, B., Werdenich, M., 2020. Organic metamorphism
819 as a key for reconstructing tectonic processes: a case study from the Austroalpine unit (Eastern Alps). *International*
820 *Journal of Earth Sciences* 109, 2235–2253. <https://doi.org/10.1007/s00531-020-01897-7>
- 821 Regenauer-Lieb, K., Rosenbaum, G., Lyakhovsky, V., Liu, J., Weinberg, R., Segev, A., Weinstein, Y., 2015. Melt
822 instabilities in an intraplate lithosphere and implications for volcanism in the Harrat Ash-Shaam volcanic field
823 (NW Arabia). *Journal of Geophysical Research* 120 (3), 1543–1558. <https://doi.org/10.1002/2014JB011403>
- 824 Ring, U., Brandon, M.T., 1999. Ductile deformation and mass loss in the Franciscan Subduction complex:
825 implications for exhumation processes in accretionary wedges. In: Ring, U., Brandon, M.T., Lister, G.S., Willett,
826 S.D. (Ed.), *Exhumation Processes: Normal Faulting, Ductile Flow and Erosion*. Geological Society of London
827 Special Publication 154, 55-86.
- 828 Ring, U., Kumerics, C., 2008. Vertical ductile thinning and its contribution to the exhumation of high-pressure
829 rocks: the Cycladic blueschist unit in the Aegean. *Journal of the Geological Society* 165, 1019-1030.
- 830 Ring, U., Bernet, M., Tulloch, A., 2015. Kinematic, finite strain and vorticity analysis of the Sisters shear zone,
831 Stewart Island, New Zealand. *Journal of Structural Geology* 73, 114-129

- 832 Ring, U., Brandon, M.T., Ramthun, A., 2001. Solution-mass-transfer deformation adjacent to the Glarus Thrust,
833 with implications for the tectonic evolution of the Alpine wedge in eastern Switzerland. *Journal of Structural*
834 *Geology* 23, 1491–1505. [https://doi.org/10.1016/S0191-8141\(01\)00015-3](https://doi.org/10.1016/S0191-8141(01)00015-3)
- 835 Sanderson, D.J., 1982. Models of strain variation in nappes and thrust sheets: a review. *Tectonophysics* 88, 201-
836 233.
- 837 Scharf, A., Handy, M.R., Ziemann, M.A., Schmid, S.M., 2013. Peak-temperature patterns of polyphase
838 metamorphism resulting from accretion, subduction and collision (eastern Tauern window, European alps) – a
839 study with Raman microspectroscopy on carbonaceous material (RSCM). *Journal of Metamorphic Geology* 31,
840 863–880. <https://doi.org/10.1111/jmg.12048>
- 841 Schmalholz, S., Duretz, T., 2015. Shear zone and nappe formation by thermal softening, related stress and
842 temperature evolution, and application to the Alps. *Journal of Metamorphic Geology* 33(8), 887–908.
843 <https://doi.org/10.1111/jmg.12137>
- 844 Schneider, J., Corsini, M., Peila, A., Lardeaux, J., 2014. Thermal and mechanical evolution of an orogenic wedge
845 during Variscan collision: an example in the Maures-Tanneron Massif (SE France). *Geological Society of London*
846 405, 313-331. <https://doi.org/10.1144/SP405.4>
- 847 Schott, B., Yuen, D., Schmeling, H., 2000. The significance of shear heating in continental delamination. *Physics*
848 *of the Earth and Planetary Interiors* 118, 273-290.
- 849 Seno, S., Dallagiovanna, G., Vanossi, M., 1998. From finite strain data to strain history: a model for a sector of
850 the Ligurian Alps, Italy. *Journal of Structural Geology* 20, 573-585. [https://doi.org/10.1016/S0191-](https://doi.org/10.1016/S0191-8141(97)00104-1)
851 [8141\(97\)00104-1](https://doi.org/10.1016/S0191-8141(97)00104-1)
- 852 Simonetti, M., Carosi, R., Montomoli, C., Cottle, J.M., Law, R.D., 2020a. Transpressive deformation in the
853 southern European variscan belt: new insights from the Aiguilles Rouges massif (western Alps). *Tectonics* 39.
854 <https://doi.org/10.1029/2020TC006153>
- 855 Simonetti, M., Carosi, R., Montomoli, C., Corsini, M., Petroccia, A., Cottle, J.M., Iaccarino, S., 2020b. Timing
856 and kinematics of flow in a transpressive dextral shear zone, Maures Massif (Southern France). *International*
857 *Journal of Earth Sciences* 109, 2261–2285. <https://doi.org/10.1007/s00531-020-01898-6>
- 858 Simonetti, M., Carosi, R., Montomoli, C., Law, R.D., Cottle, J.M., 2021. Unravelling the development of regional-
859 scale shear zones by a multidisciplinary approach: The case study of the Ferriere-Mollières Shear Zone (Argentera
860 Massif, Western Alps). *Journal of Structural Geology* 149, 104399. <https://doi.org/10.1016/j.jsg.2021.104399>.

- 861 Simpson, C. De Paor, D.G., 1993. Strain and kinematic analysis in general shear zones. *Journal of Structural*
 862 *Geology* 15, 1–20. [https://doi.org/10.1016/0191-8141\(93\)90075-1](https://doi.org/10.1016/0191-8141(93)90075-1)
- 863 Skrzypek, E., 2021. First- and second-order Raman spectra of carbonaceous material through successive contact
 864 and regional metamorphic events (Ryoke belt, SW Japan). *Lithos* 388–389, 106029.
 865 <https://doi.org/10.1016/j.lithos.2021.106029>.
- 866 Steck, A., 2008. Tectonics of the Simplon massif and Lepontine gneiss dome: deformation structures due to
 867 collision between the underthrusting European plate and the Adriatic indenter. *Swiss Journal of Geosciences* 101,
 868 515–546. <https://doi.org/10.1007/s00015-008-1283-z>
- 869 Steck, A., Della Torre, F., Keller, F., Pfeifer, H.-R., Hunziker, J., Masson, H., 2013. Tectonics of the Lepontine
 870 Alps: ductile thrusting and folding in the deepest tectonic levels of the Central Alps. *Swiss Journal of Geosciences*
 871 106, 427–450. <https://doi.org/10.1007/s00015-013-0135-7>
- 872 Stipp, M., Stünitz, H., Heilbronner, R., Schmid, S.M., 2002. Dynamic recrystallization of quartz: correlation
 873 between natural and experimental conditions. *Geological Society of London, Special Publications* 200, 171–190.
 874 <https://doi.org/10.1144/GSL.SP.2001.200.01.11>
- 875 Takeuchi, C.S., Fialko, Y., 2012. Dynamic models of interseismic deformation and stress transfer from plate
 876 motion to continental transform faults. *Journal of Geophysical Research* 117, B05403.
 877 <https://doi.org/10.1029/2011JB009056>
- 878 Thielmann, M., Kaus, B.J.P., 2012. Shear heating induced lithospheric-scale localization: does it result in
 879 subduction? *Earth and Planetary Science Letters* 359, 1–13. <https://doi.org/10.1016/j.epsl.2012.10.002>
- 880 Thigpen, J. R., Ashley, K. T., Law, R. D., 2017. Evaluating kinematic displacement rate effects on transient
 881 thermal processes in thrust belts using coupled thermomechanical finite-element models. In: Law, R. D., Thigpen,
 882 J. R., Merschat, A. J., Stowell H. H. (Ed.), *Linkage and feedbacks in orogenic systems* 213, 1–23. *Geological*
 883 *Society of America Memoir*. [https://doi.org/10.1130/2017.1213\(01\)](https://doi.org/10.1130/2017.1213(01))
- 884 Thigpen, J. R., Ashley, K. T., Mako, C., Law, R. D., Spencer, B., 2021. Interplay between crustal-scale thrusting,
 885 high metamorphic heating rates, and the development of inverted thermal-metamorphic gradients: Numerical
 886 models and examples from the Caledonides of northern Scotland. *Tectonics*, 40, e2021TC006716.
 887 <https://doi.org/10.1029/2021TC006716>
- 888 Thigpen, J.R., Law, R.D., Lloyd, G.E., Brown, S.J., Cook, B., 2010. Deformation temperatures, vorticity of flow
 889 and strain symmetry in the Loch Eriboll mylonites, NW Scotland: implications for the kinematic and structural
 890 evolution of the northernmost Moine Thrust zone. *Geological Society of London, Special Publications* 335, 623–
 891 662. <https://doi.org/10.1144/sp335.26>

- Thigpen, J.R., Law, R.D., Loehn, C., Strachan, R.A., Tracy, R., Lloyd, G., Roth, B., Brown, S., 2013. Thermal structure and tectonic evolution of the Scandian orogenic wedge, Scottish Caledonides: Integrating geothermometry, deformation temperatures, and kinematic-thermal modeling. *Journal of Metamorphic Geology* 31, 813–842. <https://doi.org/10.1111/jmg.12046>
- Tikoff, B., Fossen, H., 1995. The limitations of three-dimensional kinematic vorticity analysis. *Journal of Structural Geology* 17, 1771–1784.
- Vai, G.B., Coccozza, T., 1974. Il “postgotlandiano” sardo, unità sinorogenica ercinica. *Bollettino della Società Geologica Italiana* 93, 61–72.
- Vidal, O., Lanari, P., Munoz, M., Bourdelle, F., De Andrade, V., 2016. Deciphering temperature, pressure and oxygen-activity conditions of chlorite formation, *Clay Minerals*, 51, 615–633 <https://doi.org/10.1180/claymin.2016.051.4.06>
- Vitale, S., Mazzoli, S., 2008. Heterogeneous shear zone evolution: the role of shear strain hardening/softening. *Journal of Structural Geology* 30, 1383–1395.
- Vitale Brovarone, A., Beyssac, O., Malavieille, J., Molli, G., Beltrando, M., Compagnoni, R., 2013. Stacking and metamorphism of continuous segments of subducted lithosphere in a high-pressure wedge: The example of Alpine Corsica (France). *Earth-Science Reviews* 116, 35–56. <https://doi.org/10.1016/j.earscirev.2012.10.003>
- Vitale Brovarone, A., Tumiatì, S., Piccoli, F., Ague, J. J., Connolly, J. A. D., Beyssac, O., 2020. Fluid-mediated selective dissolution of subducting carbonaceous material: Implications for carbon recycling and fluid fluxes at forearc depths, *Chemical Geology* 549, 119682, <https://doi.org/10.1016/j.chemgeo.2020.119682>
- Vollmer, F.W., 2015. EllipseFit 3.2. <https://www.frederickvollmer.com/ellipsefit/>
- Wallis, S.R., Platt, J.P., Knott, S.D., 1993. Recognition of synconvergence extension in accretionary wedges with examples from the Caledonian Arc and the Eastern Alps. *American Journal of Science* 293, 463–495. <https://doi.org/10.2475/ajs.293.5.463>
- Wang, L., Cao, D.Y., Peng, Y.W., Ding, Z.Y., Li, Y., 2019b. Strain-induced graphitization mechanism of coal-based graphite from Lutang, Hunan Province, China. *Minerals* 9(10), 617. <https://doi.org/10.3390/min9100617>
- Waters, D.J., Law, R.D., Searle, M.P., Jessup, M., 2018, Structural and thermal evolution of the South Tibetan Detachment shear zone in the Mt. Everest region, from the 1933 sample collection of L.R. Wager, in Ferrero, S., Lanari, P., Goncalves, P., and Grosch, E., eds., *Metamorphic Geology: Microscale to Mountain Belts: Geological Society of London, Special Publication 478*, 38 p., <https://doi.org/10.1144/SP478.17>

- 921 Whitney, D., Evans, B., 2010. Abbreviations for names of rock-forming minerals. *American Mineralogy* 95, 185–
922 187. <https://doi.org/10.2138/am.2010.3371>
- 923 Willis, K., Houseman, G. A., Evans, L., Wright, T., Hooper, A., 2019. Strain localization by shear heating and the
924 development of lithospheric shear zones, *Tectonophysics* 764, 62–76. <https://doi.org/10.1016/j.tecto.2019.05.010>
- 925 Yonkee, A., 2005. Strain patterns within part of the Willard thrust sheet, Idaho-Wyoming-Utah thrust belt. *Journal*
926 *of Structural Geology* 27, 1315-1343. <https://doi.org/10.1016/j.jsg.2004.06.014>
- 927 Xypolias, P., 2010. Vorticity analysis in shear zones: A review of methods and applications. *Journal of Structural*
928 *Geology* 32, 2072–2092. <https://doi.org/10.1016/j.jsg.2010.08.009>
- 929



930

931 Fig. 1: a) Geographic position and tectonic sketch map of the Sardinia Island (modified from Carmignani et al., 1994).
 932 Location of Fig. 1b is indicated; b) Schematic geological map of the Internal and External Nappe Zone in the central Sardinia.
 933 The location of Area I and Area II has been highlighted. The trace of the geological cross-section A-A''' is indicated (modified
 934 from Carmignani et al., 1994, 2015); c) Geological A-A''' cross-section along the Internal and External Nappe Zone. The
 935 deep structure of the Barbagia Synform is uncertain. The horizontal and vertical exaggeration is for both 1.5:1.

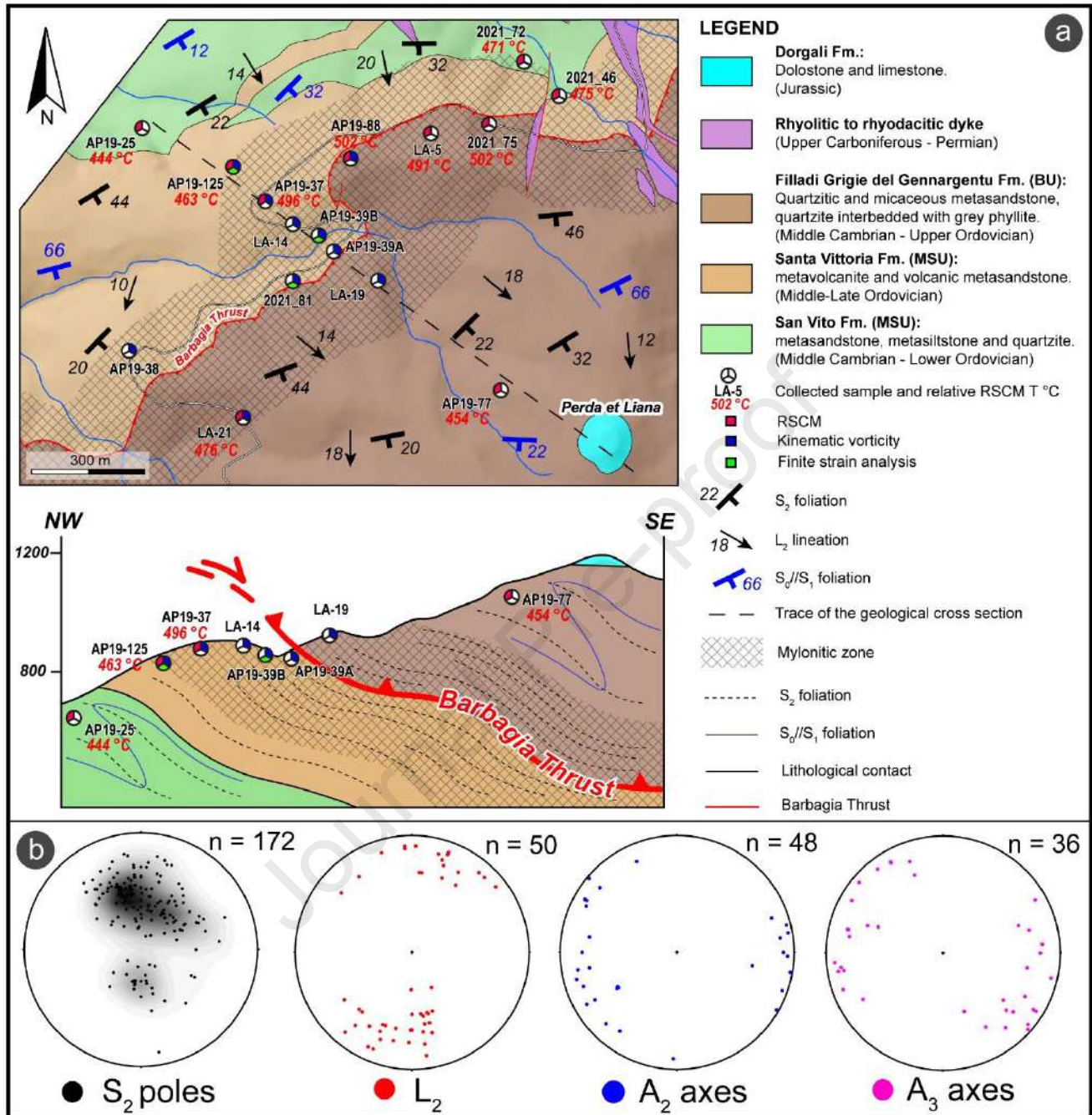


Fig. 2: a) Geological map of Area I, derived from our original fieldwork and mapping. The trace of NW-SE oriented geological cross-section, shown below (the vertical exaggeration is 2:1), is indicated. On the cross-section the selected samples locations and the corresponding type of analysis are indicated; b) Stereoplots (equal angle, lower hemisphere projections) of the main structural elements.

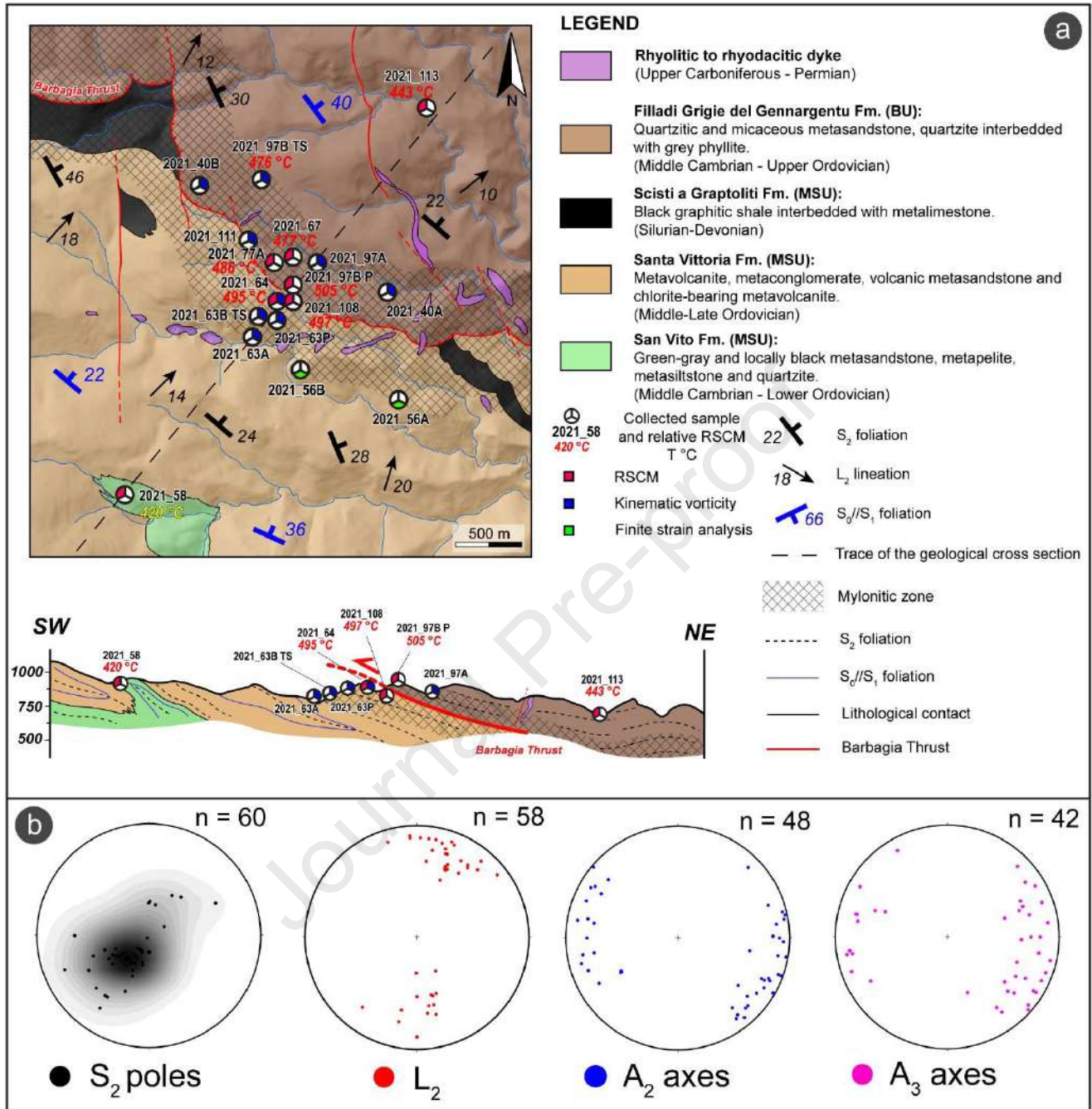


Fig. 3: a) Geological map of Area II (modified and integrated from Carosi, 2004). The trace of the NW-SE oriented geological cross-section, shown below (no vertical exaggeration) is indicated. On the cross-section the selected samples locations and the corresponding type of analysis are indicated; b) Stereoplots (equal angle, lower hemisphere projections) of the main structural elements.

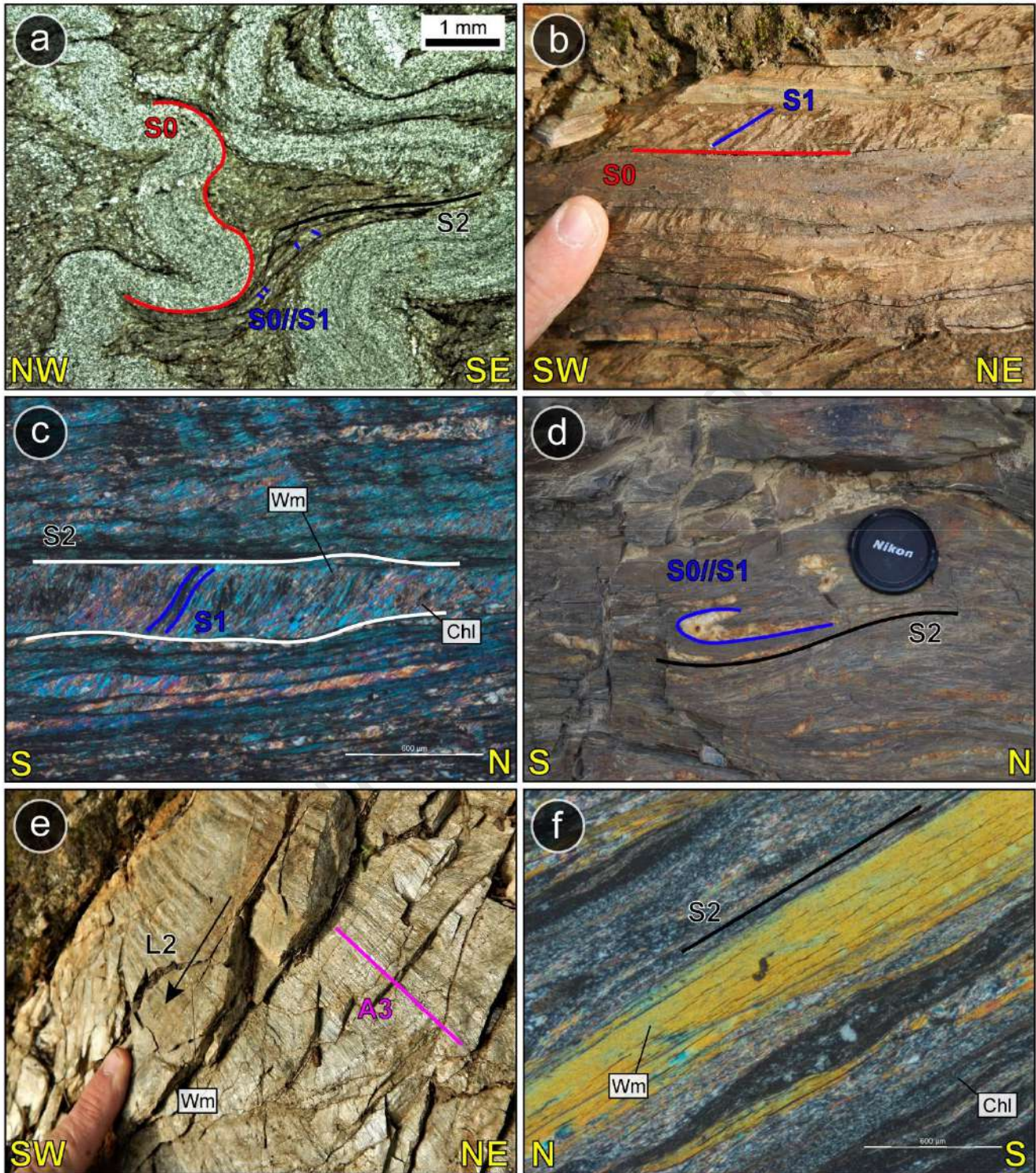
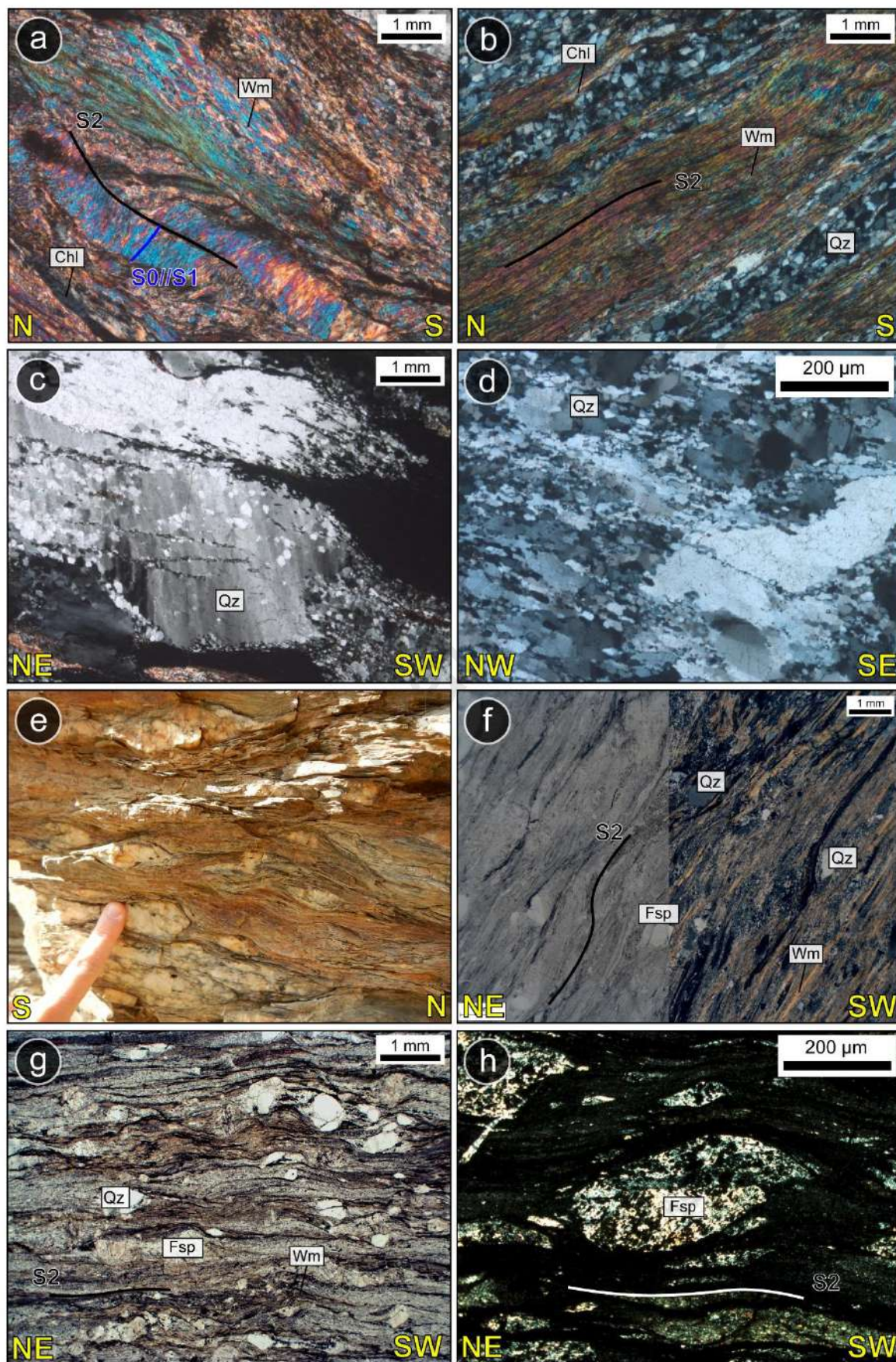


Fig. 4: a) S_2 spaced foliation with S_0/S_1 preserved in microlithons. A relict of bedding (S_0), defined by the primary compositional alternation between quartz-rich and phyllosilicate-rich levels, is recognizable (PPL: parallel-polarised light) (San Vito Fm.; FW); b) Selective S_1 foliation involving the S_0 compositional alternation in metasedimentary rock (Filladi

951 Grigie del Gennargentu Fm.; HW); c) S_2 spaced foliation at the microscale. S_1 preserved in microlithons is defined by
952 Wm+Chl (XPL: crossed-polarised light) (San Vito Fm.; FW); d) Outcrop evidence of F_2 rootless fold. S_0/S_1 foliation is
953 preserved in the hinge of F_2 folds. The S_2 cleavage is parallel to the F_2 axial plane (Filladi Grigie del Gennargentu Fm.; HW);
954 e) L_2 object lineation, defined by Wm crystals and the intersection lineation, parallel to the A_3 fold axes, are displayed (San
955 Vito Fm.; FW); f) S_2 fine-grained continuous foliation defined by Wm+Chl alternating with quartz-rich levels in
956 metasedimentary rocks (XPL) (San Vito Fm.; FW).

957



959 Fig. 5: Meso- and micro-scale features across the BT mylonitic zone. a) S_2 spaced foliation in metasedimentary rocks (San
 960 Vito Fm.; FW). Both S_1 and S_2 cleavages are defined by Wm+Chl (XPL); b) Continuous cleavage in metasedimentary rocks
 961 (Filladi Grigie del Gennargentu Fm.; HW). S_2 cleavage is defined by both quartz and phyllosilicate-rich horizons (XPL)
 962 (Filladi Grigie del Gennargentu Fm.; HW); c) quartz with small new-grains and undulose extinction indicative of BLG II
 963 mechanism (XPL) (Filladi Grigie del Gennargentu Fm.; HW); d) quartz with BLG II and minor local SGR mechanisms in a
 964 mylonite, subgrains, and new grains can be recognized (XPL) (Filladi Grigie del Gennargentu Fm.; HW); e) HW mylonites
 965 at the mesoscale: mylonitic fabric indicating a sense of shear top-to-the S (Filladi Grigie del Gennargentu Fm.); f) FW
 966 mylonite at the microscale: C'-S fabric is indicative of a top-to-the SW sense of shear (PPL and XPL) (San Vito Fm.; g) FW
 967 metavolcanoclastic mylonitic rocks. C'-S fabric and rotated porphyroclasts pointing to a top-to-the SW sense of shear (PPL)
 968 (Santa Vittoria Fm.); h) Fine-grained continuous cleavage and sigma-type porphyroclast in the FW ultramylonite indicating
 969 a top-to-the SW sense of shear (XPL) (Santa Vittoria Fm.).

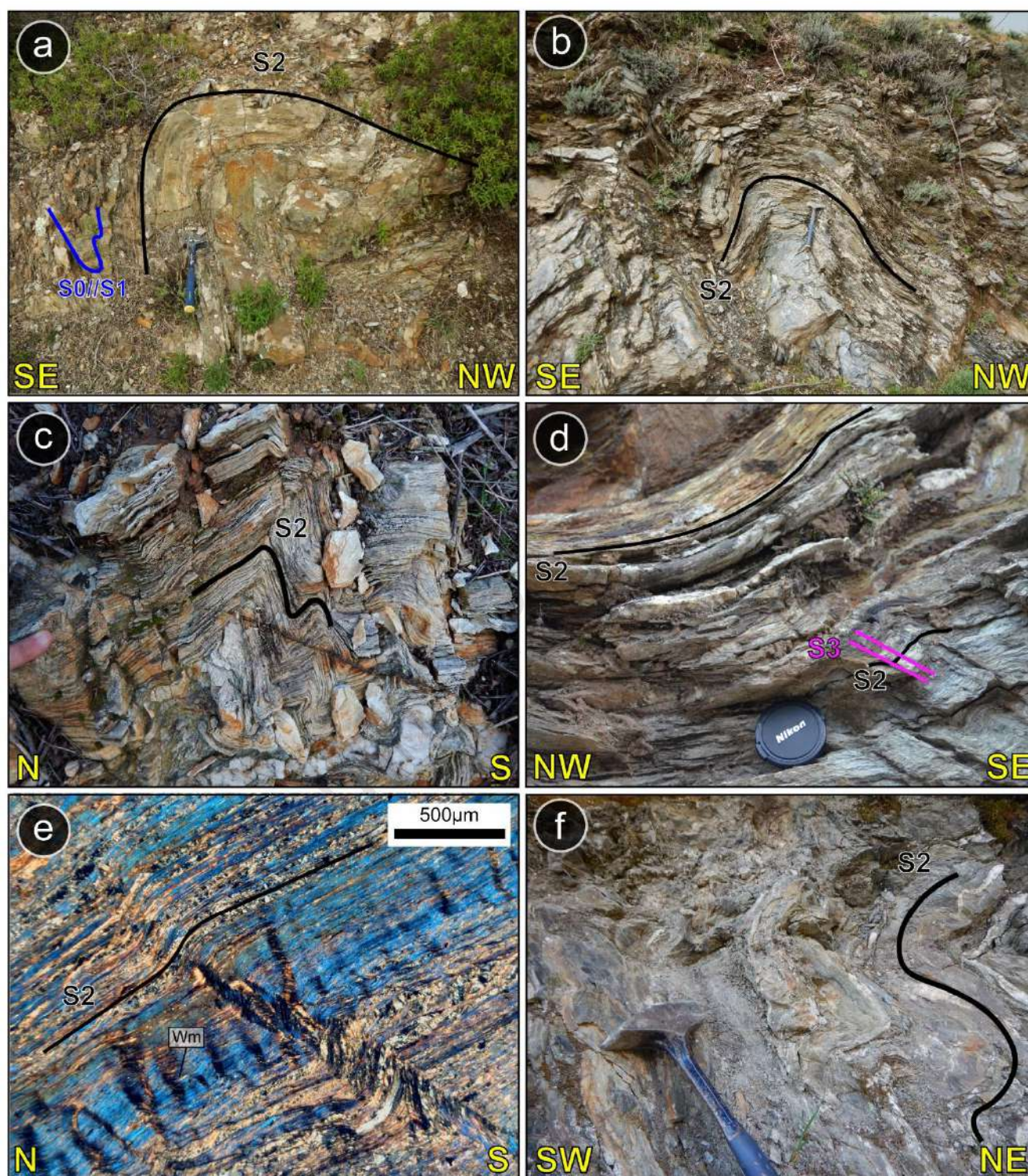
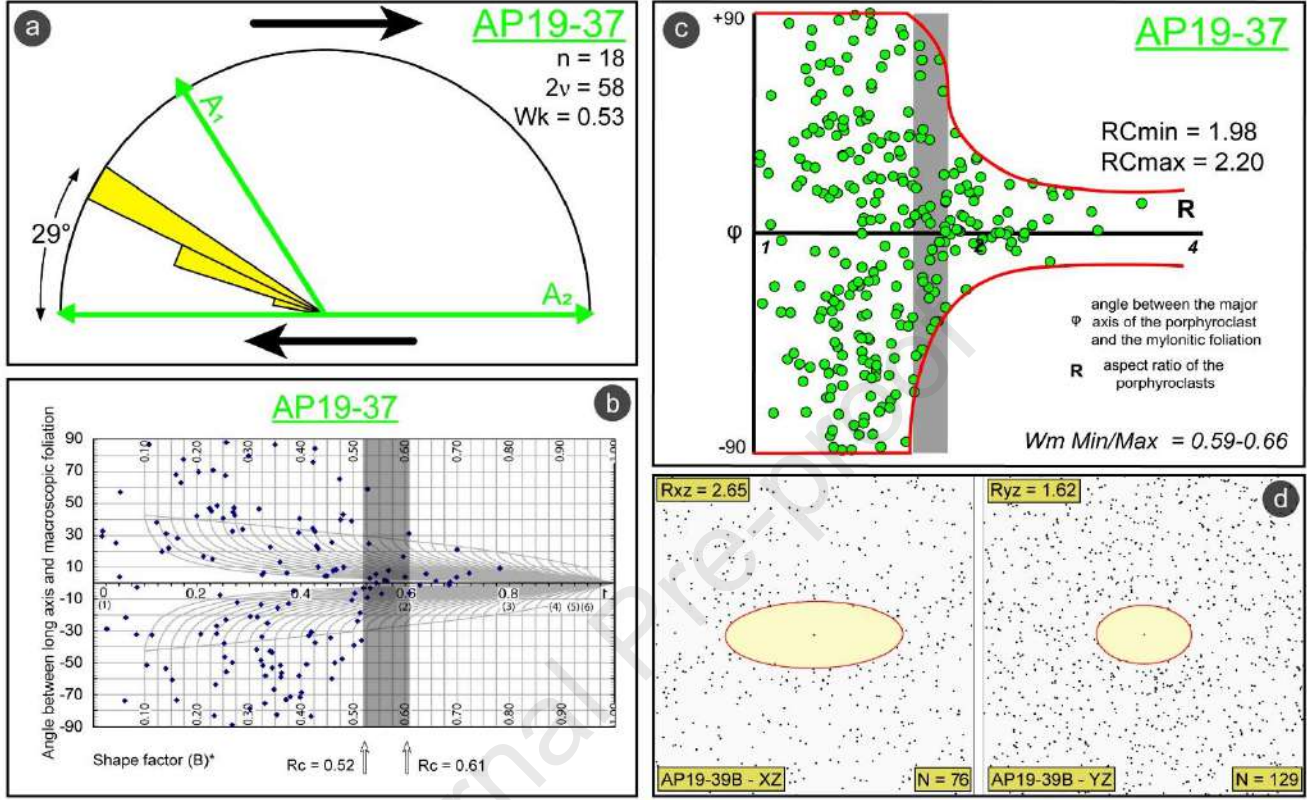


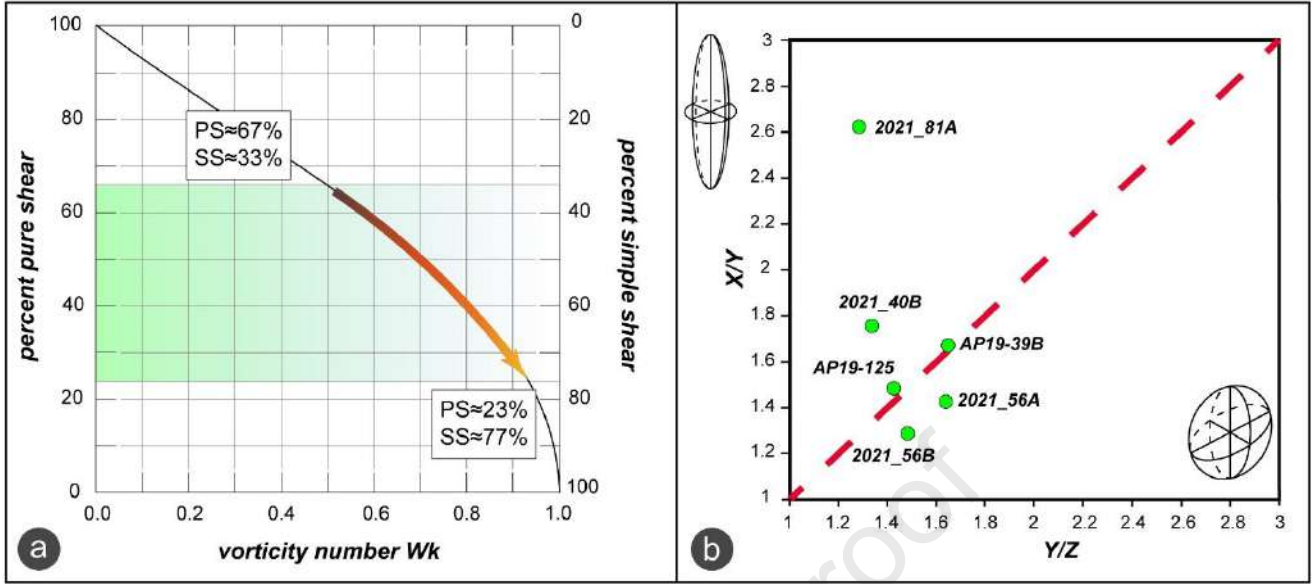
Fig. 6: Outcrop aspect of the F₃ (a) asymmetric, (b) upright and (c) kink folds, showing mainly S-SE vergence; d) S₃ spaced foliation at mesoscale developed only in less competent layers in the hinge of F₃ fold; e) Continuous S₂ foliation, defined by

973 Wm+Chl, deformed by F_3 micro-kink folds (XPL); f) Outcrop evidence of late open folds (F_4) with sub-horizontal axes and
 974 axial planes, deforming S_2 foliation.



975

976 Fig. 7: Example of vorticity analysis and finite strain results. a) Polar histogram used to derive the angle v , and the
 977 corresponding kinematic vorticity number, Wk . A_1 = flow apophysis 1; A_2 = flow apophysis 2; n = total number of data; b)
 978 and c) Example of the plots for the porphyroclasts-based methods (b=RGN; c= stable porphyroclasts method). $Rcmin$ and
 979 $Rcmax$ = minimum and maximum critical axial ratio; Wm = mean kinematic vorticity number; d) Fry diagram for the XZ and
 980 YZ sections of the finite strain ellipsoid. N = number of centers considered in the analysis. The RXZ and RYZ axial ratios are
 981 shown.



982

983 Fig. 8: a) Diagram showing the relative percentage of simple shear obtained from the selected samples of both areas. The
 984 simple shear component increases (highlighted by the arrow) according to deformation gradient; b) Flinn diagram showing
 985 the analyzed samples (green dots) finite strain results (for sample location see figure 2a, 3a).

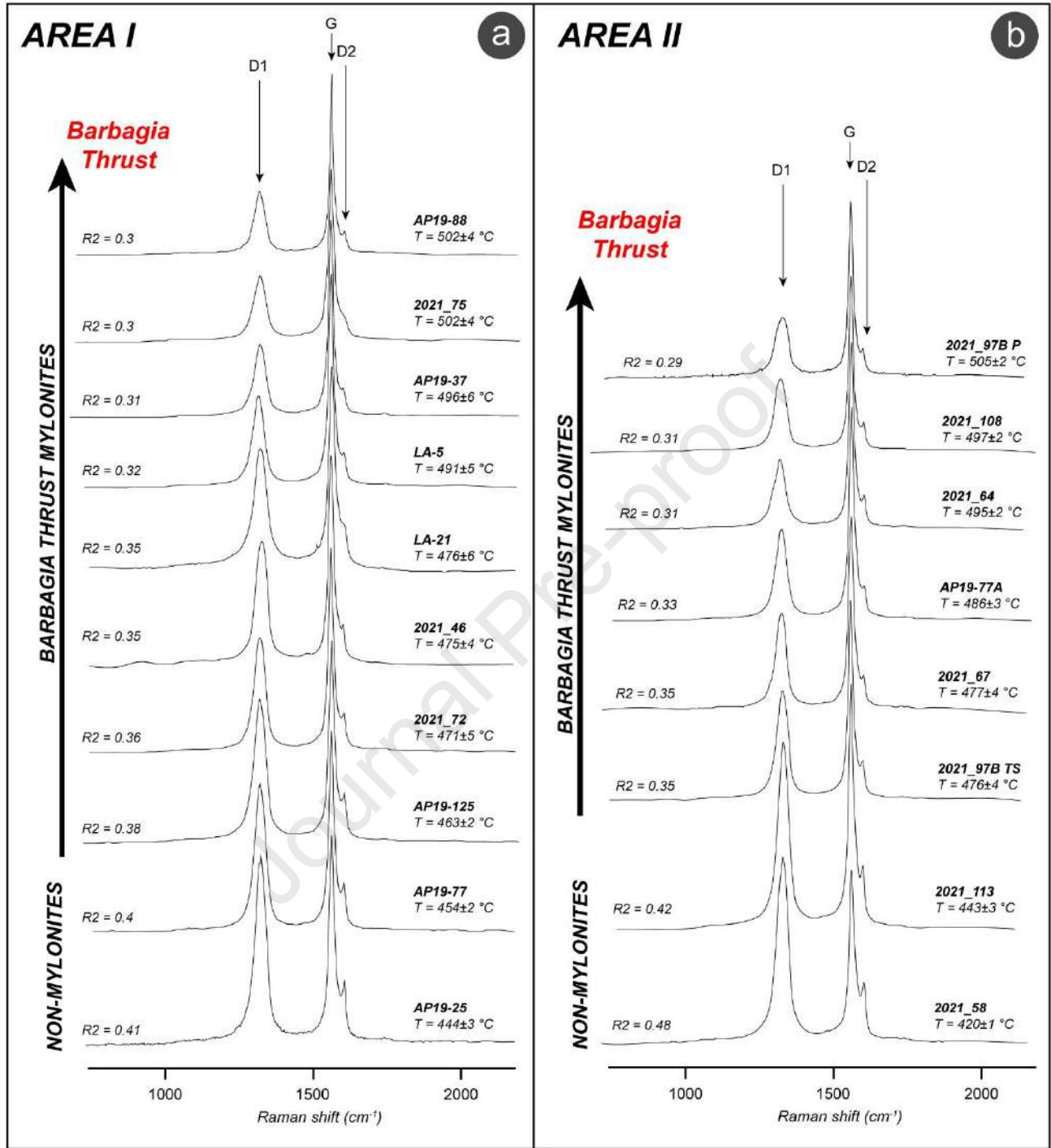
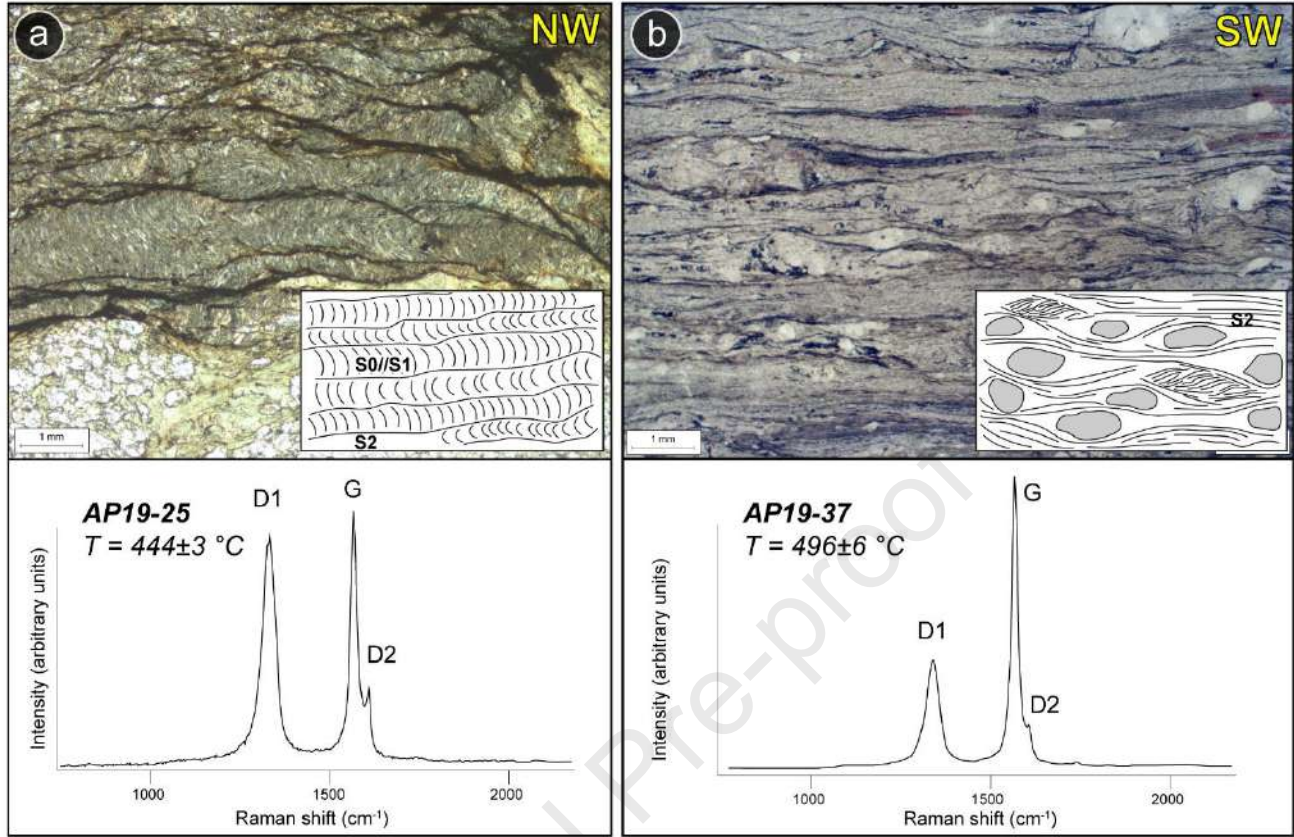


Fig. 9: Raman spectra of carbonaceous material obtained in non- and mylonitic rocks of both investigated areas for Area I (a) and Area II (b). For each spectrum, the R2 ratio and the corresponding RSCM T (°C) with the relative simplified error have been indicated. Samples are ordinated according to structural distance from the Barbagia Thrust.



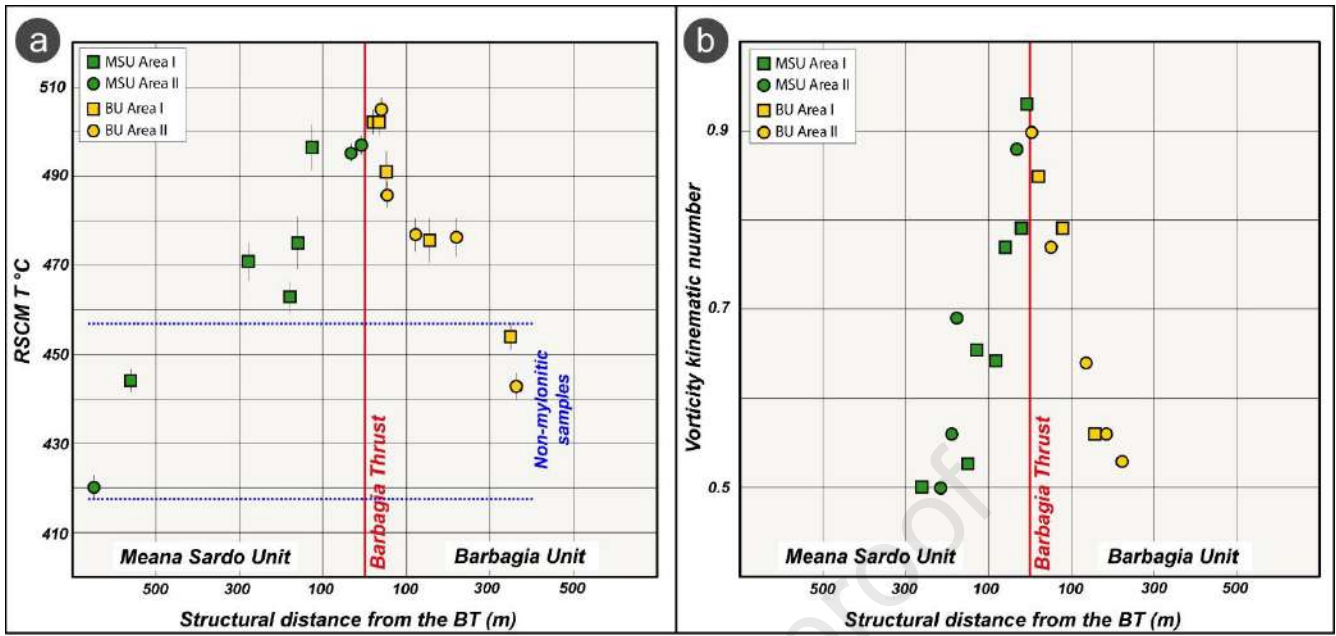
991

992

993

994

Fig. 10: Example from the Area I of the variation of RSCM temperature in different deformed rocks. Thin sections (PPL) and representative Raman spectra for carbonaceous material from FW samples AP19-25 (a) and AP19-37 (b), respectively outside and inside the mylonitic zone (see Fig. 2a for the position of the samples). Note that the RSCM T (°C) is higher in the mylonite.



995

996

997

998

Fig. 11: a) Distribution of RSCM T (°C) compared with the sample structural distance with respect to the BT. b) Distribution of estimated vorticity kinematic number against the structural distance from the BT. Both graphs show increasing RSCM T (°C) and Wk values (i.e., increase in simple shear) toward the shear zone.

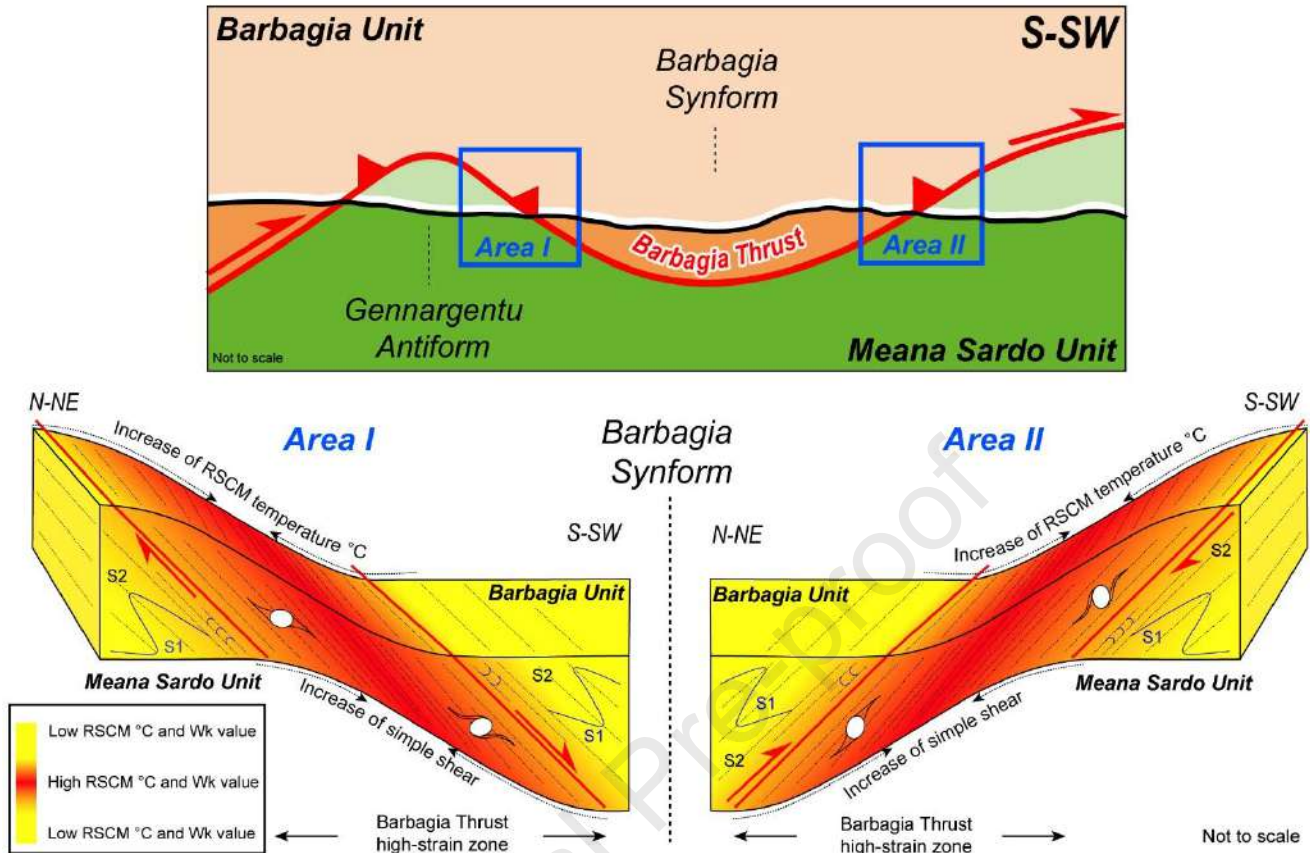


Fig. 12: On the top, the current stage of the architecture of the belt is shown by a simplified cross-section across the Internal and External Nappe Zone. We highlighted the approximated position of the investigated areas and the simplified present-day topography. The sense of shear is the same in both areas, pointing to a top-to-to-the S/SW. On the bottom, not to scale representations of the Barbagia Thrust along with the northern and southern limb of the Barbagia Synform have been displayed. The given "finite" shape is not referred to the shear displacement but due to the late fold (F_3) linked to D_3 deformation (Barbagia Synform). The progressive strain partitioning and gradient, from fold structures to a mylonitic foliation (approaching the BT high-strain zone), have been highlighted, mirrored by the increase of both simple shear and the RSCM T ($^{\circ}\text{C}$).

Area I

RSCM analysis											Kinematic vorticity and finite strain analysis													
					Aoye et al., 2010			Beyssac et al.,						RGN			Porphyroclasts method			Finite strain analysis				
SAMPLE NAME	UNIT	DISTANCE FROM THE BT (m)	n.	R2	SD	SE (°C)	RSCM °C	SD	SE (°C)	RSCM °C	N	ANGLE (°)	Wk	N	Wm	Rc min	Rc max	Wk min	Wk max	Wk mid	R _{xx}	R _{yy}	R _{xy}	K
AP19-77	BU	350	10	0.40	5.7	1.9	454	5.6	1.9	464	-	-	-	-	-	-	-	-	-	-	-	-	-	-
LA-21	BU	156	12	0.35	18.1	5.5	476	16.8	5.1	486	18	28	0.56	-	-	-	-	-	-	-	-	-	-	-
LA-19	BU	80	-	-	-	-	-	-	-	-	9	19	0.79	-	-	-	-	-	-	-	-	-	-	-
LA-5	BU	52	12	0.32	17.2	5.2	491	15.6	4.7	498	-	-	-	-	-	-	-	-	-	-	-	-	-	-
2021_75	BU	22	11	0.30	14.0	4.4	502	12.4	3.9	508	-	-	-	-	-	-	-	-	-	-	-	-	-	-
AP19-88	BU	18	11	0.30	13.4	4.2	502	11.9	3.8	508	22	16	0.85	-	-	-	-	-	-	-	-	-	-	-
AP19-39A	MSU	10	-	-	-	-	-	-	-	-	11	11	0.93	-	-	-	-	-	-	-	-	-	-	-
2021_81A	MSU	16	-	-	-	-	-	-	-	-	14	19	0.79	-	-	-	-	-	-	-	3.30	1.26	2.62	6.23
AP19-39B	MSU	60	-	-	-	-	-	-	-	-	22	20	0.77	-	-	-	-	-	-	-	2.65	1.62	1.64	1.03
AP19-38	MSU	84	-	-	-	-	-	-	-	-	18	25	0.64	-	-	-	-	-	-	-	-	-	-	-
LA-14	MSU	122	-	-	-	-	-	-	-	-	-	-	-	164	0.56 - 0.65	2.11	2.33	0.63	0.69	0.66	-	-	-	-
AP19-37	MSU	126	10	0.31	17.4	5.8	496	15.6	5.2	503	18	29	0.53	280	0.52 - 0.61	1.98	2.20	0.59	0.66	0.63	-	-	-	-
2021_46	MSU	160	15	0.35	13.5	3.6	475	12.5	3.3	483	-	-	-	-	-	-	-	-	-	-	-	-	-	-
2021_72	MSU	178	16	0.36	17.7	4.6	471	16.4	4.2	480	-	-	-	-	-	-	-	-	-	-	-	-	-	-
AP19-125	MSU	280	10	0.38	5.2	1.7	463	4.9	1.6	472	22	30	0.50	-	-	-	-	-	-	-	2.18	1.42	1.54	1.27
AP19-25	MSU	560	10	0.41	8.2	2.7	444	8.1	2.7	455	-	-	-	-	-	-	-	-	-	-	-	-	-	-

Area II

RSCM analysis											Kinematic vorticity and finite strain analysis													
					Aoye et al., 2010			Beyssac et al.,						RGN			Porphyroclasts method			Finite strain analysis				
SAMPLE NAME	UNIT	DISTANCE FROM THE BT (m)	n.	R2	SD	SE (°C)	RSCM °C	SD	SE (°C)	RSCM °C	N	ANGLE (°)	Wk	N	Wm	Rc min	Rc max	Wk min	Wk max	Wk mid	R _{xx}	R _{yy}	R _{xy}	K
2021_113	BU	360	12	0.42	8.3	2.5	443	8.2	2.5	454	-	-	-	-	-	-	-	-	-	-	-	-	-	-
2021_97B TS	BU	220	16	0.35	16.3	4.2	476	14.8	3.8	485	15	29	0.53	-	-	-	-	-	-	-	-	-	-	-
2021_97A	BU	180	-	-	-	-	-	-	-	-	17	28	0.56	-	-	-	-	-	-	-	-	-	-	-
2021_40A	BU	135	-	-	-	-	-	-	-	-	18	25	0.64	-	-	-	-	-	-	-	-	-	-	-
2021_67	BU	122	11	0.35	11.7	3.7	477	10.7	3.4	485	-	-	-	-	-	-	-	-	-	-	-	-	-	-
AP19-77A	BU	55	10	0.33	8.6	2.9	486	7.8	2.6	494	-	-	-	-	-	-	-	-	-	-	-	-	-	-
2021_40B	BU	52	-	-	-	-	-	-	-	-	12	20	0.77	-	-	-	-	-	-	-	2.42	1.36	1.78	2.17
2021_97B P	BU	40	12	0.29	6.5	2	505	5.7	1.7	511	-	-	-	-	-	-	-	-	-	-	-	-	-	-
2021_111	BU	12	-	-	-	-	-	-	-	-	7	13	0.90	-	-	-	-	-	-	-	-	-	-	-
2021_108	MSU	10	10	0.31	7.2	2.4	497	6.4	2.1	504	-	-	-	-	-	-	-	-	-	-	-	-	-	-
2021_64	MSU	35	12	0.31	5.8	1.7	495	5.2	1.6	502	14	14	0.88	-	-	-	-	-	-	-	-	-	-	-
2021_63B P	MSU	180	-	-	-	-	-	-	-	-	12	23	0.69	-	-	-	-	-	-	-	-	-	-	-
2021_63B TS	MSU	235	-	-	-	-	-	-	-	-	16	28	0.56	-	-	-	-	-	-	-	-	-	-	-
2021_63A	MSU	254	-	-	-	-	-	-	-	-	24	30	0.5	-	-	-	-	-	-	-	-	-	-	-
2021_56B	MSU	288	-	-	-	-	-	-	-	-	-	-	-	-	-	-	-	-	-	-	1.96	1.49	1.23	0.39
2021_56A	MSU	300	-	-	-	-	-	-	-	-	-	-	-	-	-	-	-	-	-	-	2.25	1.63	1.38	0.61
2021_58	MSU	650	18	0.48	5.5	1.3	420	5.7	1.4	429	-	-	-	-	-	-	-	-	-	-	-	-	-	-

Table 1: Results of the RSCM estimations (both Aoya et al. (2010) and Beyssac et al. (2002) calibrations results are indicated), kinematic vorticity, and the finite strain (see Figure 2 and Figure 3 for samples location). Samples, divided according to the corresponding tectonic unit, are listed according to the distance with respect to the BT. The number of spectra (n), mean R2 ratio (Beyssac et al., 2002) for n spectra with corresponding standard deviation (SD), and calculated temperature with standard error ($SE = SD/\sqrt{n}$) have been indicated.

[illegible][illegible]

Highlights

Temperature variations responsible for the dynamic weakening and localization of strain,

Paleothermal architecture fits with a tectonic scenario of shear heating coupled with a simple shear increase

The tectonic contact represents a full-fledged boundary that divides the internal sector of the Internal sector of the wedge to the external one

Declaration of competing interest

The authors declare that they have no competing financial interests or personal relationships that could have appeared to influence the work reported in this paper.